NASA Technical Paper 3377

August 1993

Quantitative Mapping of Pore Fraction Variations in Silicon Nitride Using an Ultrasonic Contact Scan Technique

Don J. Roth,
James D. Kiser,
Suzanne M. Swickard,
Steven A. Szatmary,
and David P. Kerwin

NASA

NASA Technical Paper 3377

1993

Quantitative Mapping of Pore Fraction Variations in Silicon Nitride Using an Ultrasonic Contact Scan Technique

Don J. Roth,
James D. Kiser,
and Suzanne M. Swickard
Lewis Research Center
Cleveland, Ohio

Steven A. Szatmary
and David P. Kerwin
Cleveland State University
Cleveland, Ohio

National Aeronautics and Space Administration

Office of Management
Scientific and Technical Information Program

Contents

1.0 Summary

An ultrasonic scan procedure using the pulse-echo contact configuration was employed to obtain maps of pore fraction variations in sintered silicon nitride samples in terms of ultrasonic material properties. Ultrasonic velocity, attenuation coefficient, and reflection coefficient images were obtained simultaneously over a broad band of frequencies (e.g., 30 to 110 MHz) by using spectroscopic analysis. Liquid and membrane (dry) coupling techniques and longitudinal and shear-wave energies were used. The major results include the following: Ultrasonic velocity (longitudinal and shear wave) images revealed and correlated with the extent of average through-thickness pore fraction variations in the silicon nitride disks. Attenuation coefficient images revealed pore fraction nonuniformity due to the scattering that occurred at boundaries between regions of high and low pore fraction. Velocity and attenuation coefficient images were each nearly identical for machined and polished disks, making the method readily applicable to machined materials. Velocity images were similar for wet and membrane coupling. Maps of apparent Poisson's ratio constructed from longitudinal and shear-wave velocities quantified Poisson's ratio variations across a silicon nitride disk. Thermal wave images of a disk indicated transient thermal behavior variations that correlated with observed variations in pore fraction and velocity and attenuation coefficients.

2.0 Introduction

Traditional nondestructive evaluation (NDE) imaging methods applicable to the characterization of high-performance materials, such as vehicular engine ceramics and composites, include x-radiography, ultrasonic imaging, and thermal inspection (ref. 1). In their standard configurations, these methods measure an amplitude of transmission of the respective energy used. These methods provide an efficient, quasi-quantitative measure of material homogeneity but may lack the precision necessary for microstructure evaluation for high-performance materials (refs. 2 and 3). The use of materials in demanding high-performance applications will require detailed quantitative knowledge of microstructural and compositional variability for defining acceptable levels of variability and for rejecting those materials and processes that yield sample-to-sample and within-sample variations likely to result in unacceptable property (e.g., strength, thermal conductivity, or oxidation resistance) variations. Variability must be precisely characterized either directly in terms of property measurement or indirectly through microstructural characterization where microstructure-property relations have been previously established. In support of the latter, quantitative NDE methods for the determination of the global microstructural state are currently being developed and refined to aid in advanced materials development efforts (refs. 4 to 7).

Repeated, uniformly spaced ultrasonic contact measurements have been successful in previous studies for quantifying and mapping inhomogeneity in various ceramics (SiC, Al_2O_3, $YBa_2Cu_3O_7$) and metals *in terms of ultrasonic material properties* (refs. 6 and 8 to 12). Such ultrasonic material properties include velocity, reflection coefficient, and attenuation coefficient. In most cases, velocity mapping has been the preferred ultrasonic property map due to its repeatable nature, relatively low sensitivity to material surface condition and edge effects (ref. 13), and relative ease of quantitatively interpreting results in terms of microstructural features (ref. 14). Spatial microstructural variations previously characterized in terms of ultrasonic velocity include variations in pore fraction, granular texture, and residual stress (refs. 9, 10, and 12). Reflection coefficient and attenuation coefficient maps derived from contact scanning have been used to a lesser extent for characterizing spatial variations in polycrystalline materials (ref. 6) because of an expected sensitivity to surface condition (ref. 15) and edge effects (ref. 13) and more difficulty in quantitatively interpreting results in terms of microstructrual features (ref. 6).

In this study, the ultrasonic contact pulse-echo method was used in an automated scanning configuration in an attempt to quantify and map nonuniformity in polished and machined sintered silicon nitride (Si_3N_4) disks containing distinct regions of high pore fraction formed during sintering. Here, the configuration was significantly (hardware and software) modified from that of previous approaches (refs. 9, 10, and 16). Modification allowed the examination of any two-dimensional, complex-shaped (e.g., circular, tensile shaped) sample by using small-diameter probes. The modification also allowed the use of dry as well as wet coupling and thus shear as well as longitudinal wave energies. Reflection coefficient, attenuation coefficient, and velocity maps of the Si_3N_4 disks were formed over a wide frequency range (e.g., 30 to 110 MHz) by using spectral analysis after acquisition of ultrasonic

waveform data. These three types of ultrasonic property maps were examined to determine which ultrasonic property map is most effective in characterizing nonununiformity and the nature of the correlation, if any, between different ultrasonic property maps. Spectral analysis was employed to determine if inhomogeneity was a function of frequency and to characterize elastic (dispersion) behavior for Si_3N_4. Additionally, maps of Poisson's ratio for a disk were constructed from longitudinal and shear-wave velocity images. Thermal wave imaging and Vickers microhardness measurements were used to determine if physical behavior variations correlated with pore fraction variations that had been characterized metallographically and in ultrasonic images. A positive correlation would indicate the usefulness of the ultrasonic measurement as an aid for predicting physical behavior.

The authors wish to thank the Metallographic Support Staff for their help in sample preparation and analysis, James R. Bodis for his help in obtaining ultrasonic C-scan and microfocus radiography images, and Maurice Bales of Bales Scientific, Inc., and Elliot Cramer of NASA Langley Research Center for their help in obtaining thermal wave images.

3.0 Background

3.1 Importance of Si_3N_4

The past 20 years have seen significant interest in ceramic materials for high-temperature structural applications, such as vehicular engines (refs. 17 and 18). Si_3N_4 is a candidate material for such applications because of its low density, high melting point, high strength, and resistance to wear, thermal shock, and creep (refs. 17 and 18). Si_3N_4 has application as a monolithic material, a toughened monolithic material, and the matrix material in ceramic matrix composites (refs. 17 to 19). The Si_3N_4 used in this study can also be considered a model material for demonstrating the capabilities of the modified ultrasonic contact scan technique.

3.2 Relationships Between Ultrasonic Properties and Experimental Variables

The significant material-behavior-related variables in this study were ultrasonic frequency and pore fraction. A detailed discussion follows concerning expected relationships between these variables and the ultrasonic reflection coefficient, attenuation coefficient, and velocity for Si_3N_4 when the contact pulse-echo experimental technique (refs. 20 and 21) is used. In this technique, an ultrasonic pulse generated by a piezoelectric crystal is propagated into a buffer rod-couplant-sample configuration (figs. 1(a) and (b)). In this investigation, the buffer rod, the couplant, and the sample are fused silica (SiO_2), diffusion pump fluid, and Si_3N_4, respectively. The ultrasound reflects off the front and back surfaces of the sample and travels back to the crystal. Figures in the immediate upcoming sections show the expected frequency and pore fraction dependence of velocity, reflection coefficient, and attenuation coefficient for the following conditions: contact pulse-echo configuration, frequency range of 30 to 110 MHz, pore fraction

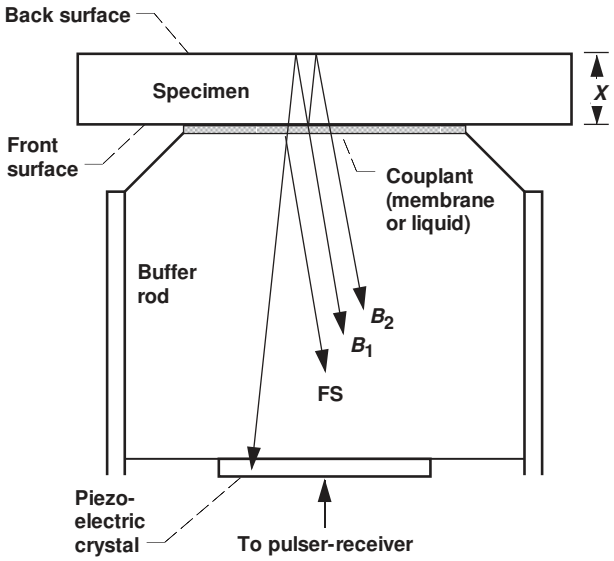

(a) Diagram of buffer rod-couplant-sample pulse-echo contact configuration.

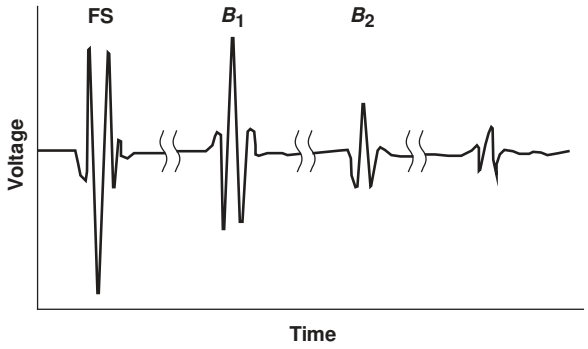

(b) Resulting waveforms for pulse-echo contact technique.

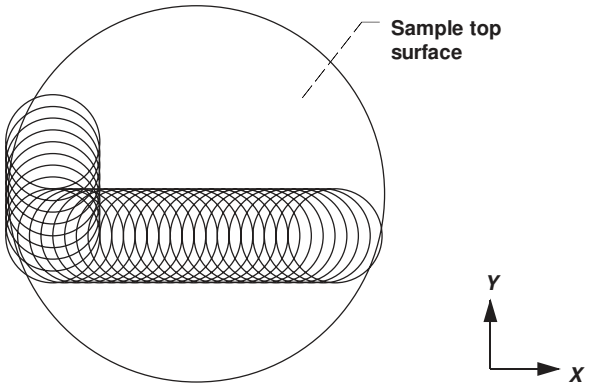

(c) Schematic (top view) of ultrasonic contact scan procedure showing examples of successive transducer positions along *X*- and *Y*-dimensions of sample.

Figure 1.—Ultrasonic measurement method (FS = front-surface reflection; B_1 = first back-surface reflection; B_2 = second back-surface reflection).

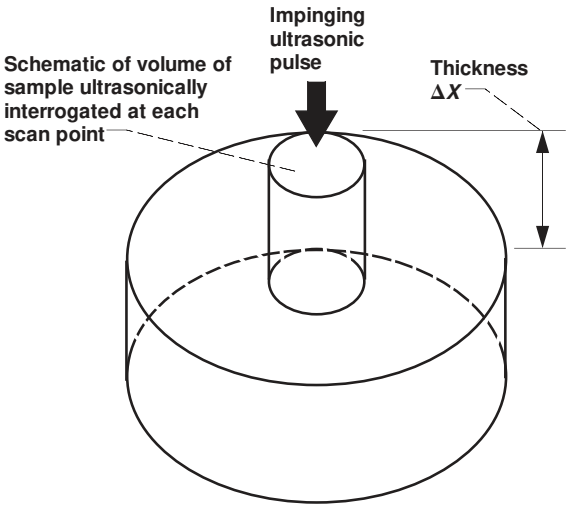

(d) Schematic (three-dimensional view) showing volume of sample ultrasonically interrogated at each scan point for velocity and attenuation coefficient measurements.

Figure 1.—Concluded.

range of 0 to 0.1, pore radius of 1 μm, and ultrasonic velocity in fully dense Si_3N_4 of 1.12 cm/μsec.

Velocity.—Brittle materials, such as monolithic ceramics, generally exhibit linear elastic behavior at room temperature (ref. 22), and therefore dispersion (velocity varying with frequency, ref. 23) and frequency-dependent attenuation are not expected to be present to the extent that they would be for viscoelastic media, such as polymeric materials, where energy absorption is the dominant attenuation mechanism (refs. 24 and 25). However, the presence of defects in ceramics, such as pores, grain boundaries, and dislocations, can lead to frequency-dependent effects because ultrasonic energy is scattered from such defects. For the case of multiple scattering where the scatterers are cavities, a low cavity concentration exists, and Rayleigh scattering predominates, Sayers has shown the following relationship for velocity (refs. 26 and 29):

$$V = V_o\left\{1 + 0.5P\left[A + B(ka)^2\right]\right\} \qquad (1)$$

where A and B are constants that depend on the ratio of longitudinal to shear-wave velocity, $ka = 2\pi af/V$, P is pore fraction, V_o is the velocity in a fully dense material containing no pores, V is the velocity in a material containing pores, a is pore radius, and f is frequency. For the Si_3N_4 in this study, $V_L/V_S \approx 1.8$; thus $A = -1.1$ and $B = -1.8$ according to Sayers' analysis (ref. 26). Equation (1) thus becomes

$$V_{Si_3N_4} = 1.12\ cm/\mu\sec\left\{1 + 0.5P \times\left[-1.1 - 1.8\left(\frac{2\pi fa}{1.12\ cm/\mu\sec}\right)^2\right]\right\} \qquad (2)$$

Figures 2(a) and (c) show the expected theoretical dependence of the ultrasonic velocity in Si_3N_4 ($V_{Si_3N_4}$) on pore fraction and frequency by using equation (2). The velocity $V_{Si_3N_4}$ is expected to linearly decrease with increasing pore fraction (from 1.12 cm/μsec at full density to about 1.06 cm/μsec for 0.1 pore fraction) for

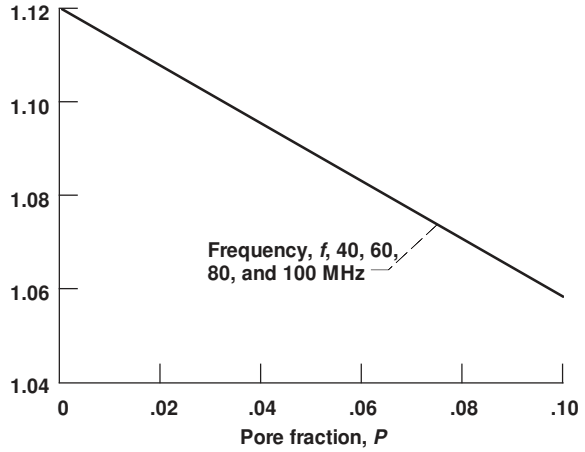

(a) Theoretical velocity versus pore fraction for various frequencies (eq. (2)).

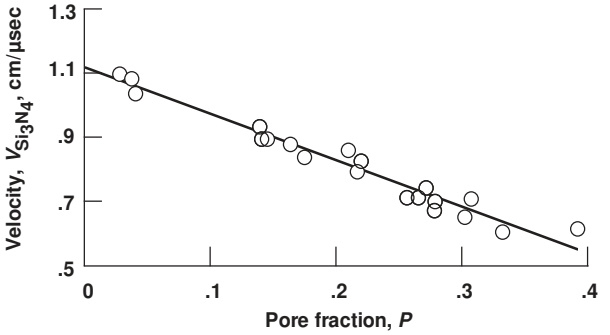

(b) Measured velocity versus pore fraction where $V_{Si_3N_4}$ = –0.014 x Percent porosity + 1.12 was previously observed empirically (0.98 correlation coefficient; ref. 14).

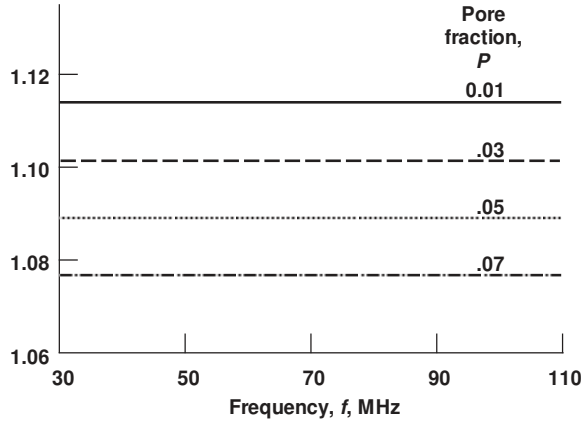

(c) Theoretical velocity versus frequency for various pore fractions (eq. (2)).

Figure 2.—Expected dependence of ultrasonic velocity in Si_3N_4 on pore fraction and frequency.

all frequencies and to show little dependence on frequency over the specified frequency range. Figure 2(b) shows velocity versus pore fraction for Si_3N_4, where the relationship $V_{Si_3N_4} = -0.014 \times \text{Percent porosity} + 1.12$ was previously observed empirically (0.98 correlation coefficient) in reference14.

Reflection coefficient.—The theoretical expression for the buffer rod-couplant-sample (BCS) pressure reflection coefficient is (ref. 28)

$$R = \frac{\left(1-\frac{Z_1}{Z_3}\right)\cos\left[\frac{2\pi f(\delta X)}{V_2}\right] + j\left(\frac{Z_2}{Z_3}-\frac{Z_1}{Z_2}\right)\sin\left[\frac{2\pi f(\delta X)}{V_2}\right]}{\left(1+\frac{Z_1}{Z_3}\right)\cos\left[\frac{2\pi f(\delta X)}{V_2}\right] + j\left(\frac{Z_2}{Z_3}+\frac{Z_1}{Z_2}\right)\sin\left[\frac{2\pi f(\delta X)}{V_2}\right]} \tag{3}$$

where f is the frequency of the ultrasonic transducer; V_2 is the velocity of sound in the couplant layer; Z_1, Z_2, and Z_3 are the acoustic impedance of the buffer rod, couplant, and sample, respectively; and δX is the couplant thickness. The magnitude of this complex expression is (ref. 15)

$$|R| = \left\{\frac{\left(1-\frac{Z_1}{Z_3}\right)^2\cos^2\left[\frac{2\pi f(\delta X)}{V_2}\right] + \left(\frac{Z_2}{Z_3}-\frac{Z_1}{Z_2}\right)^2\sin^2\left[\frac{2\pi f(\delta X)}{V_2}\right]}{\left(1+\frac{Z_1}{Z_3}\right)^2\cos^2\left[\frac{2\pi f(\delta X)}{V_2}\right] + \left(\frac{Z_2}{Z_3}+\frac{Z_1}{Z_2}\right)^2\sin^2\left[\frac{2\pi f(\delta X)}{V_2}\right]}\right\}^{\frac{1}{2}} \tag{4}$$

The acoustic impedance of the sample Z_3 is given by (ref. 13)

$$Z_3 = \rho_3 V_3 \tag{5}$$

where ρ_3 and V_3 are the sample density and velocity, respectively. As the number of scatterers at the material surface increases, it is expected that ρ_3 and V_3 will be altered, changing Z_3 and thus altering R. The manner in which R is expected to change with material change depends on the compositional nature of the scatterer (pore, second-phase inclusion, etc.). For example, if the scatterers are pores, Z_3 is expected to decrease with increasing volume fraction of pores as ρ_3 and V_3 are effectively decreased according to (ref. 14)

$$Z_3 = \rho_{0,3}(1-P)V_{0,3}(1-P) \tag{6}$$

where $\rho_{0,3}$, $V_{0,3}$, and P are the density of a sample with no pores, the velocity in a sample with no pores, and the pore fraction in the sample, respectively. Substituting the right side of equation (6) into equation (4) for Z_3 and substituting the values $\delta X = 1$ μm, $Z_{SiO_2} = 1.31$ g/cm-sec, $Z_{couplant} = 0.15$ g/cm-sec, $\rho_{0,Si_3N_4} = 3.3$ g/cm^3, and $V_{0,Si_3N_4} = 1.12$ g/cm^3 in equation (4) allows the magnitude of the reflection coefficient $R_{Si_3N_4}$ for the buffer (SiO_2) - couplant (Dow Corning 704) - sample (Si_3N_4) configuration used in this study to be expressed in terms of frequency and pore fraction. Figures 3(a) and (b) show the expected dependence of the theoretical reflection coefficient $R_{Si_3N_4}$ on pore fraction and frequency for the BCS configuration of this study (couplant thickness, 1 μm). The reflection coefficient $R_{Si_3N_4}$ is expected to linearly decrease with increasing pore fraction for all frequencies and more steeply at lower frequencies and to increase with increasing frequency for all pore fractions.

Changing the pore fraction may also affect the average surface roughness, which may then alter the average couplant thickness δX and change $R_{Si_3N_4}$. Figure 3(c) shows the frequency dependence of $R_{Si_3N_4}$ for several different couplant thicknesses for frequencies from 30 to 110 MHz. For a given frequency, $R_{Si_3N_4}$ increases with increasing couplant thickness. For a given couplant thickness, $R_{Si_3N_4}$ increases with increasing frequency except for larger couplant thicknesses such as 5 μm, where $R_{Si_3N_4}$ initially increases slightly with increasing frequency and then begins to decrease slightly with increasing frequency at about 75 MHz.

Attenuation coefficient.—A theory has been developed for attenuation due to grain scattering from equiaxed grains in a single-phase, fully dense polycrystalline solid. This theory predicts that attenuation is a function of average grain size D, sonic wavelength λ, and frequency f and that this functionality depends on the ratio of sonic wavelength to grain size. Table I reviews the frequency dependence of the attenuation coefficient and the scattering mechanisms for polycrystalline materials (ref. 13). Most materials have a range of grain sizes and contain additional scatterers besides grain boundaries, such as pores, second-phase inclusions, and dislocations, that affect the attenuation coefficient.

The two-phase scattering theory developed by Truell for the case where scattering from individual scatterers is independent relates the frequency and the size and number of spherical scatterers to the attenuation coefficient α according to (refs. 27 and 29)

$$\alpha = \frac{1}{2} n_o \gamma \tag{7}$$

where n_o is the number of scatterers per unit volume and γ is the scattering cross section, which is a function of frequency and scatterer radius (refs. 27 and 29). The normalized scattering cross section γ_N is defined as (refs. 27 and 29)

$$\gamma_n = \frac{\gamma}{\pi a^2} \tag{8}$$

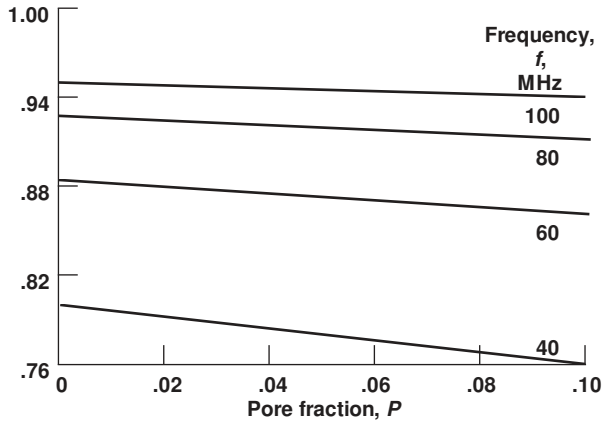

(a) Reflection coefficient versus pore fraction for various frequencies. (Couplant thickness, 1 μm.)

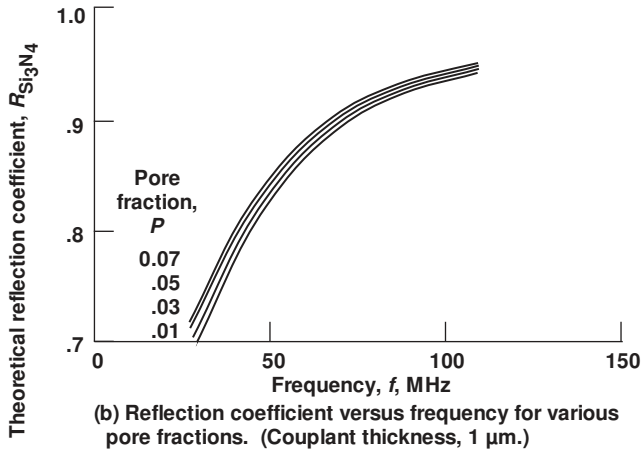

(b) Reflection coefficient versus frequency for various pore fractions. (Couplant thickness, 1 μm.)

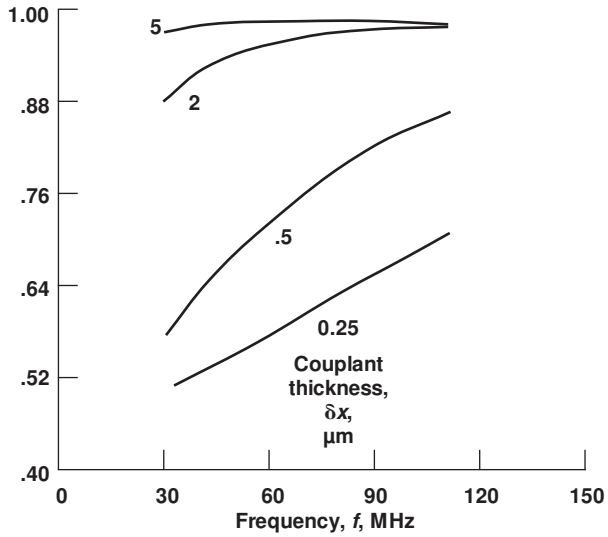

(c) Reflection coefficient versus frequency for various couplant thicknesses (eq. (4)).

Figure 3.—Expected dependence of theoretical BCS reflection coefficient on pore fraction, frequency, and couplant thickness for buffer of SiO_2, couplant of Dow Corning 704 oil, and Si_3N_4 sample.

TABLE I.—FREQUENCY DEPENDENCE OF ATTENUATION COEFFICIENT AND SCATTERING MECHANISMS FOR POLYCRYSTALLINE MATERIALS

[Experimental constants C_i are dependent on grain, geometric and elastic anisotropy, density, and longitudinal and shear-wave velocity factors.]

Wavelength/ grain size relation	Attenuation mechanism	Attenuation coefficient
Independent	True absorption	$\alpha_a = C_a f$
$\lambda >> D$	Rayleigh scattering	$\alpha_R = C_R D^3 f^4$
$\lambda \sim D$	Phase scattering	$\alpha_p = C_p D f^2$
$\lambda << D$	Diffusion scattering	$\alpha_d = C_d / D$

where a here is the scatterer radius. Reference 27 used the two-phase scattering theory to show that the attenuation coefficient due to scattering from cavities and inclusions increases with increasing frequency.

Reference 30 has calculated relative changes in the normalized scattering cross section due to scattering from pores in Si_3N_4 as a function of wavenumber times scatterer radius ka, as shown in figure 4(a). Since $ka = (2\pi af)/(V_{Si_3N_4})$, where $V_{Si_3N_4}$ is the velocity of ultrasound in Si_3N_4, relative change in the normalized scattering cross section is a function of frequency for a given pore radius and $V_{Si_3N_4}$. Thus, it is possible to estimate changes in the Si_3N_4 attenuation coefficient as a function of pore concentration (number of pores per cubic centimeter) and changes in frequency by using the following methodology and figure 4(a):

(1) Assume a constant $V_{Si_3N_4}$ of 1.08 cm/μsec and an average pore radius a of 1 μm (or 0.0001 cm). Then, the x axis in figure 4(a) becomes $(5.8\times10^{-4}\ \text{sec})f$, where f is in megahertz.

(2) Select a frequency range over which it is desired to determine attenuation coefficient changes (e.g., 30 to 110 MHz).

(3) From the curve shown in figure 4(a), relative changes in normalized scattering cross section can be determined for changes (increases) in frequency, and a relationship can be derived between $\Delta\gamma_N$ and Δf. A relationship was derived by using nonlinear regression analysis with a power function model $\Delta\gamma_N = b_1\left(\Delta f^{b_2}\right) + b_3$, forcing the b_2 exponent to be 0.5 (the curve shape in fig. 4(a) approximates $\gamma_N=(ka)^{0.5}$). For an f of 40 to 110 MHz (corresponding to a Δf of 10 to 80 MHz from a reference frequency of 30 MHz),

$$\Delta\gamma_{N_{Si_3N_4}} = 0.3396\left(\Delta f^{0.5}\right) - 0.6352 \qquad (9)$$

where $\Delta\gamma_N$ is in nepers (1 neper = 8.686 dB) and Δf is in megahertz. This relationship, shown in figure 4(b), has a coefficient of determination of 0.9996 and a final sum of squares residuals of 0.0013.

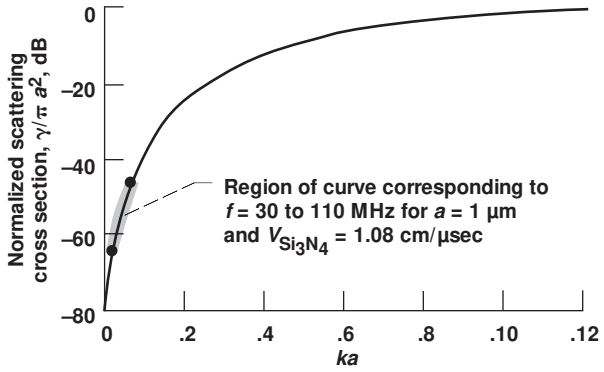

(a) Relative changes in normalized scattering cross section due to scattering from pores in Si_3N_4 as a function of wavenumber times scatterer radius *ka*. From reference 30.

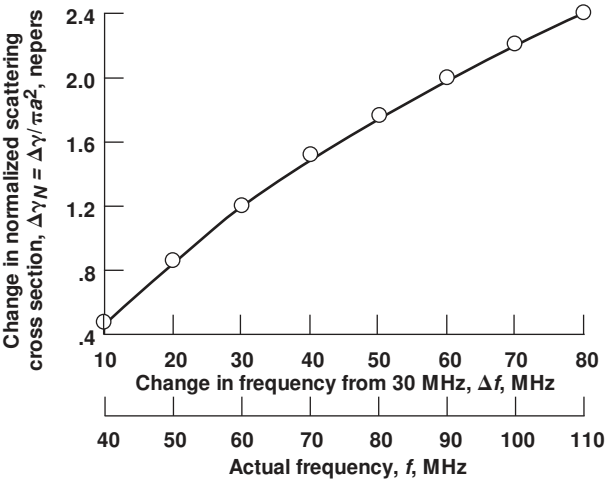

(b) Expected changes in normalized scattering cross section as function of change in frequency from 30 MHz (corresponding to frequency of 40 to 110 MHz for pore radius of 1 μm and velocity in Si_3N_4($V_{Si_3N_4}$) of 1.08 cm/μsec (derived from fig. 4(a)).

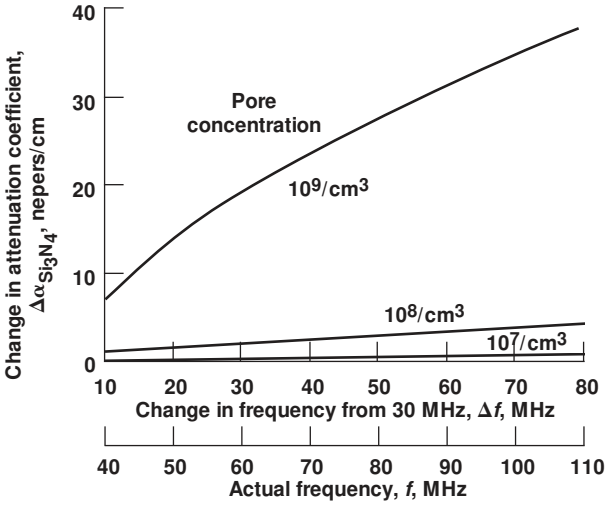

(c) Expected dependence of changes in $\alpha_{Si_3N_4}$ ($\Delta\alpha_{Si_3N_4}$) due to scattering from pores on positive changes in frequency from 30 MHz for several pore concentrations (eq. (12)).

Figure 4.—Expected changes in normalized scattering cross section and attenuation coefficient for Si_3N_4.

From equation (7), for constant n_o, changes in attenuation coefficient as a function of changes in scattering cross section can be expressed as

$$\Delta\alpha = \frac{1}{2} n_o \Delta\gamma \tag{10}$$

Rearranging equation (8) and substituting for γ in equation (10) gives

$$\Delta\alpha = \frac{10^{-8}\,\mathrm{cm}^2}{2} \pi n_o \Delta\gamma_N \tag{11}$$

Substituting the right side of equation (9) into equation (11) gives

$$\Delta\alpha_{SI_3N_4} = \left(\frac{10^{-8}\,\mathrm{cm}^2}{2}\right)\pi n_o\left[(0.3396)\Delta f^{0.5} - 0.6352\right] \tag{12}$$

where $\Delta\alpha_{Si_3N_4}$ is in nepers per centimeter and Δf is in megahertz. This relationship ignores the scattering conditions and frequency relationships shown in table I and just takes into account the shape of the curve in figure 4(b). From the ratio of the sonic wavelength (~200 μm) to the average scatterer (grain and pore) size (~1 μm) observed for the Si_3N_4 used in this study, one would predict Rayleigh scattering (α proportional to f^4). Figure 4(c) shows the expected dependence of *changes* in $\alpha_{Si_3N_4}$ ($\Delta\alpha_{Si_3N_4}$) on positive *changes* in frequency Δf from 30 MHz, assuming that pore scattering is the sole cause of attenuation for several different values of pore concentration (number of pores per cubic centimeter) n_o. The $\alpha_{Si_3N_4}$ is expected to increase with increasing frequency for any pore concentration, but the change only becomes significant for $n_o \geq 10^8$ pores/cm^3.

For nonindependent scattering (i.e., multiple scattering conditions where the scatterers become sufficiently dense and closely spaced and where the wavelength becomes comparable to the scatterer size), equation (7) cannot be used to predict the attenuation coefficient (ref. 29).

3.3 Ultrasonic Measurements

Velocity.—Velocity can be determined in several ways by using the pulse-echo configuration. In this study, cross-correlation and phase methods were used by applying frequency-domain signal processing techniques. In the cross-correlation method, the time delay τ_o between the back-surface-reflected pulses $B_1(t)$ and $B_2(t)$ (figs. 1(a) and (b)) was obtained by cross-correlating the pulses with digital signal processing (ref. 21), and the velocity V was obtained from τ_o and the sample thickness X according to (ref. 21)

$$V = 2\frac{X}{\tau_o} \tag{13}$$

Velocity determined from cross-correlation is essentially a pulse velocity because the entire wave train (containing a broad band of frequencies) is considered in the calculation. Cross-correlation is a preferred method for determining velocity, since it produces accurate velocities even with noisy signals (ref. 21). If pulse smearing occurs owing to dispersion- and/or frequency-dependent attenuation, phase methods (ref. 31) where the velocity is determined for a particular frequency may yield more accurate results. The frequency-dependent phase velocity is given by (ref. 13)

$$V(f) = \frac{(2X)2\pi f}{\Delta\theta}, \quad \Delta\theta = \theta_1 - \theta_2 \tag{14}$$

where

$$\theta_1(f) = \tan^{-1}\left\{\frac{\mathrm{Im}\left[B_1(f)\right]}{\mathrm{Re}\left[B_1(f)\right]}\right\} \tag{15}$$

$$\theta_2(f) = \tan^{-1}\left\{\frac{\mathrm{Im}\left[B_2(f)\right]}{\mathrm{Re}\left[B_2(f)\right]}\right\} \tag{16}$$

where f is frequency and $B_1(f)$ and $B_2(f)$ are the Fourier transformations of the time-domain pulses $B_1(t)$ and $B_2(t)$, respectively.

Attenuation coefficient.—The frequency-dependent attenuation coefficient for the pulse-echo configuration is given by (refs. 6 and 13)

$$\alpha(f) = \frac{1}{2X}\ln\left[\frac{|B_1(f)||R(f)|}{|B_2(f)|}\right] \tag{17}$$

where $|R(f)|$ is the frequency-dependent reflection coefficient

$$|R(f)| = \frac{|FS_2(f)|}{|FS_1(f)|} \tag{18}$$

f is frequency, $|FS_1(f)|$ and $|FS_2(f)|$ are the Fourier magnitude spectra of the time-domain pulses $FS_1(t)$ and $FS_2(t)$ without and with the sample present on the buffer rod, respectively, and $|B_1(f)|$ and $|B_2(f)|$ are the Fourier magnitude spectra of the time-domain pulses $B_1(t)$ and $B_2(t)$, respectively.

The errors associated with velocity, reflection coefficient, and attenuation coefficient measurements obtained by using the contact pulse-echo method are discussed in appendix A.

4.0 Experiment

4.1 Si_3N_4 Samples

In this investigation, seven β-Si_3N_4 disk-shaped samples (labeled SN1 to SN7) approximately 3.5 cm in diameter and 0.3 cm thick were manufactured. Details of the fabrication process are given in appendix B. The Si_3N_4 disks were 3.24 ± 0.03 g/cm^3 (> 98 percent theoretical density) as determined from immersion density measurements. From quantitative image analysis at 400× and 800×, pore dimensions were found to range from ≤1 μm (~90 percent of the pores) to as large as 10 μm with an average of approximately 1 μm. Grain dimensions for representative plasma-etched (ref. 32) sections of samples ranged from approximately 0.5 to 10 μm, with an average grain dimension of approximately 1 μm from scanning electron microscopy (SEM) analysis at 2000× to 10 000×.

At the locations where disk separators (setters) had touched the disks during sintering, visibly lighter colored regions (relative to the surrounding regions on the disks) were noted. In some cases, three such regions were apparent on each side of the disk (fig. 5). For one of the disks, no such regions were visible. It was deter-mined that these lighter areas contained a significantly higher volume fraction of pores than did the surrounding regions (fig. 6). Also, the central sections of the disks were generally more porous than the edge regions. Figures 7(a) and (b) show the percent of porosity on the surface and the average percent of porosity for lines through a section

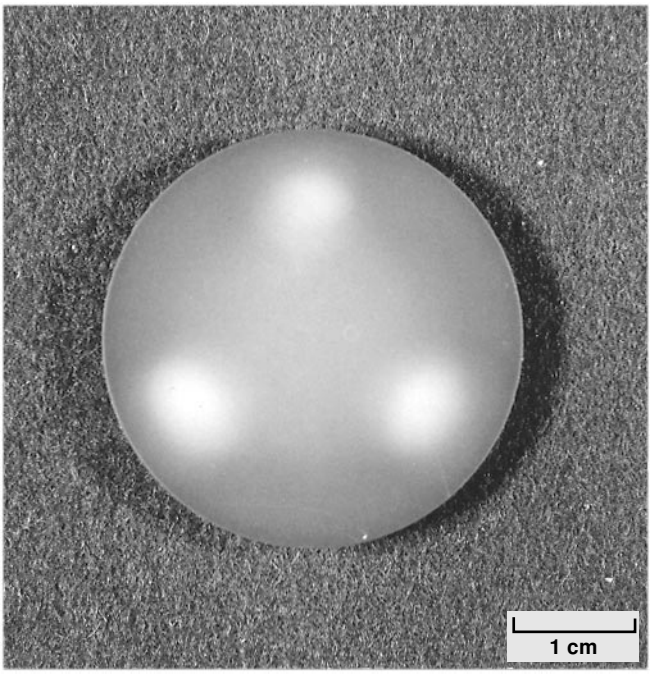

Figure 5.—Disk SN6 showing three visibly lighter colored regions (relative to surrounding regions). The other side of this disk showed the same pattern but offset 60°.

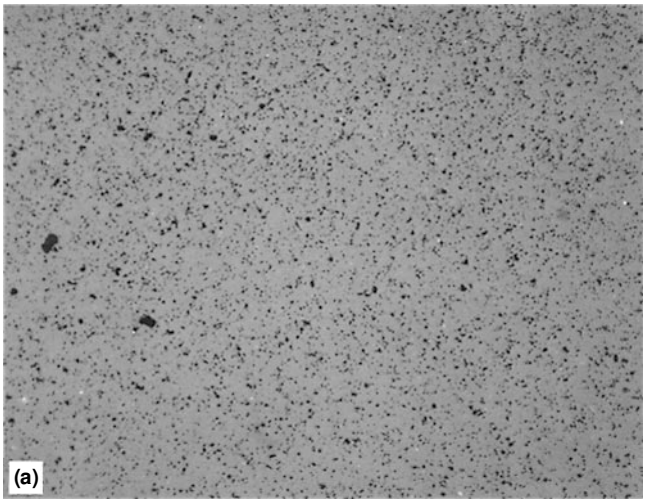

(a) Lighter colored, more porous region.

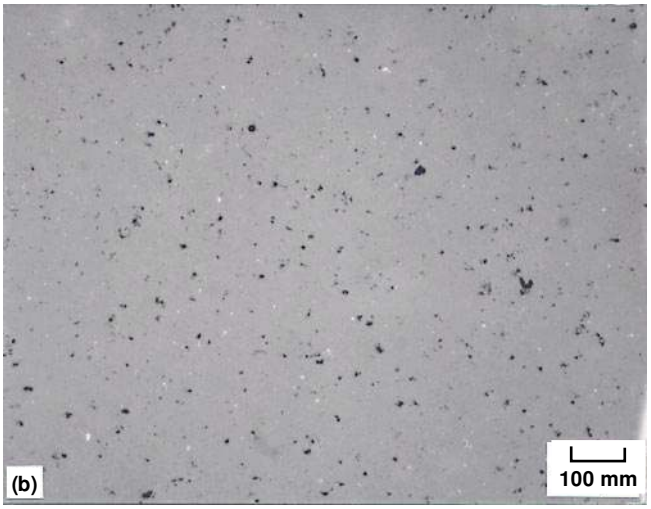

(b) Surrounding darker colored, less porous region.

Figure 6.—Photomicrographs of disk SN2.

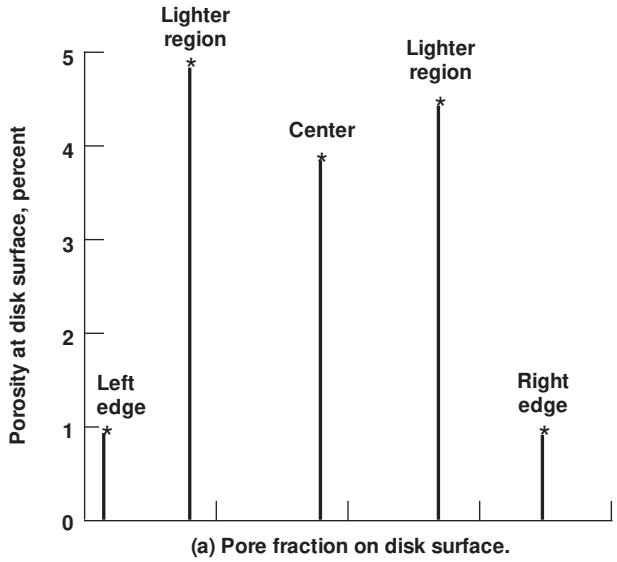

(a) Pore fraction on disk surface.

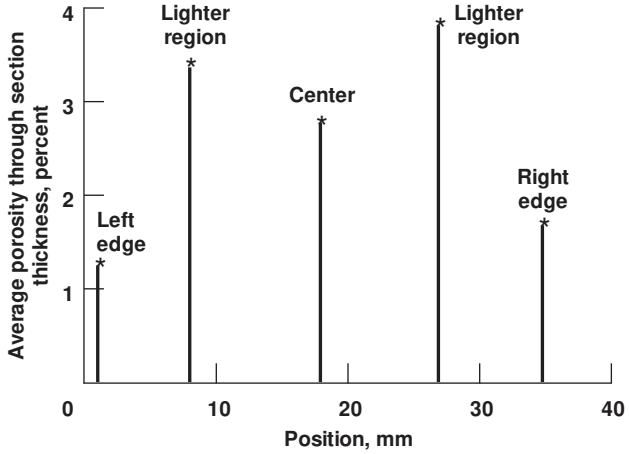

(b) Average through-thickness pore fraction at selected positions of disk SN2.

Figure 7.—Pore fraction profiles from quantitative image analysis at 800x of disk SN2 for various locations.

thickness, respectively, from quantitative image analysis at 800× of disk SN2 for various locations. Figures 8(a) and (b) show representative profiles of percent of porosity versus depth through the thickness for the lighter colored and darker colored surrounding regions, respectively.

Energy-dispersive and wavelength-dispersive x-ray scans showed no chemical (silicon, nitrogen, oxygen, yttrium, or boron) differences between the high-pore-fraction region and the surrounding regions. SEM analysis revealed no obvious grain size distribution differences between the high-pore fraction region and the surrounding regions. For one sample area examined in disk SN2, an yttria-rich glass phase was identified at grain boundaries that was approximtely 30 percent less prevalent in the high-pore-fraction region (~0.09 volume fraction glass-rich phase) than in the surrounding region (~0.12 volume fraction glass-rich phase). For the same area, an approximately 5× difference in pore fraction was noted between the high-pore-fraction region (~0.05 pore fraction) and the surrounding region (~0.01 pore fraction). In some cases, a glass-like material was observed at the bottom of and lining the pores. This material was not identified by using x-ray diffraction and energy-dispersive spectroscopy. A trace amount of an iron silicide phase was also identified at the grain boundaries. Figure 9 shows typical surface profiles for machined and polished surfaces of the Si_3N_4 disks. Machined disk surfaces were characterized by less than 1-μm peak-to-peak roughness. No differences in surface condition were observed between polished regions at a disk center and at a high-pore-fraction area.

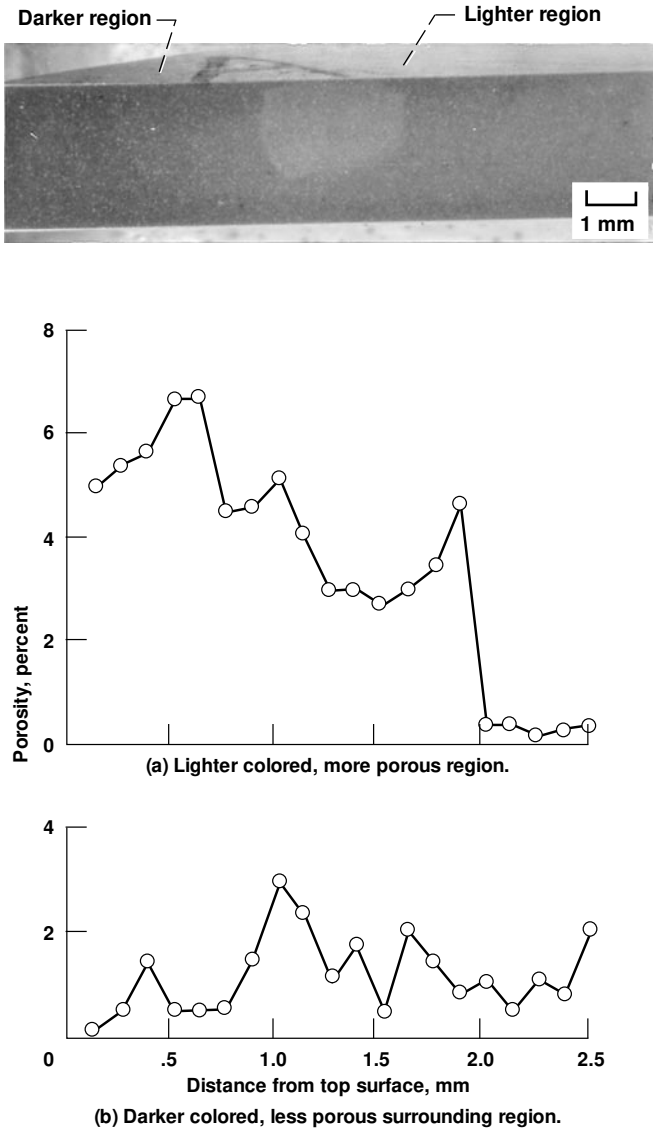

Figure 8.—Pore fraction profiles from quantitative image analysis at 800x of pore fraction versus depth through thickness for disk SN2

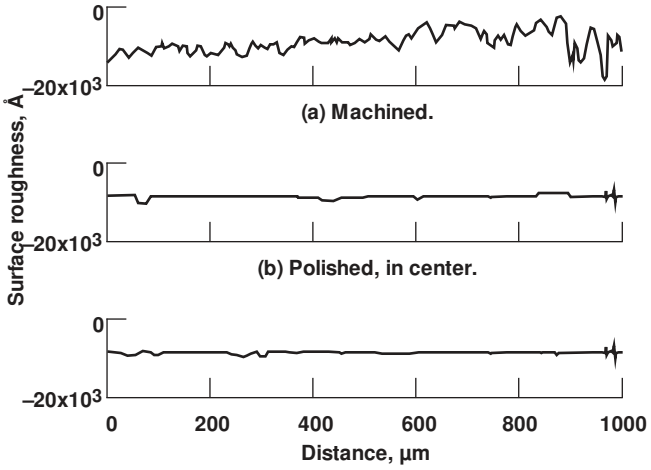

Figure 9.—Typical surface profiles for surfaces of Si_3N_4 disks.

4.2 Ultrasonic Contact Scanning

Ultrasonic measurements using the pulse-echo contact technique were obtained over an ordered array of points across the entire surface of each Si_3N_4 sample disk by means of an automated scanning technique (fig. 1). A single transducer in combination with spectral analysis allowed complete material characterization over a wide band of frequencies. This method results in considerable time savings over scanning using discrete frequency techniques. The scan technique was hardware and software modified from that of previous approaches (refs. 9, 10, and 16) to allow the scanning of entire samples without probe damage due to movement over sample edges (ref. 16), the use of transducer probes having buffer rod faces as small as 0.25 in. (0.6 cm) in diameter, and the use of membrane (dry) coupled (allowing shear-wave scans) as well as liquid (wet) coupled measurements.

The sample disks were mounted in a Lucite holder in preparation for scanning. Each scan consisted of a 47- by 41-grid of measurements with each measurement separated from the next by 1 mm. Scans were run twice in most cases to verify reproducibility. Scanning was accomplished through the use of computer-controlled *x*-, *y*-, and *z*-micropositioner tables that were used (1) to position the sample and holder under the transducer probe, (2) to raise the sample and holder so that the probe was in contact with the sample (the contact force on the probe for each measurement in a scan was 12 ± 0.1 lb for wet-coupled scans and 20 ± 0.1 lb for dry-coupled scans; the couplant layer thus should be approximately uniform for all measurements in the scan), (3) to bring the sample away from the probe after the measurement was made, and (4) to reposition the sample in the *x*- or *y*-direction (1-mm increment) for the next measurement. Echo waveforms from the sample front and back surfaces were digitized (512-point horizontal and 512-point vertical resolution), averaged over 64 waveforms, and stored. Each waveform was digitized at the voltage gain setting that allowed use of the full vertical resolution capability of the digitizer.

Digitized waveforms were Fourier transformed and subsequently processed to yield ultrasonic properties. Beam-spreading diffraction corrections were made to the amplitude spectra of each echo according to the method of Papadakis (ref. 33). (The effect of diffraction on the phase of the ultrasonic waveforms is small, and no corrections to phase were made (ref. 24). Ultrasonic images were constructed over a wide band of frequencies (e.g., 30 to 110 MHz, at 10-MHz intervals) from reflection coefficent, attenuation coefficient, and phase velocity values obtained at each scan point. One cross-correlation velocity image for each scan was also

constructed. The velocity and attenuation coefficient images can be thought of as two-dimensional projections representing averaged microstructural information for the volume of sample scanned (fig. 1(d)). A computer program was written to allow continuous image formation at discrete frequencies and subsequent storage on an optical disk. A continuous scale consisting of 256 shades of gray (or color) and linear interpolation between points allowed the display of spatial variations in these ultrasonic properties. A data clipping or filtering scheme was performed to remove faulty property values resulting from incorrect digitization and edge effects. Failure to apply the filtering resulted in misleading images and poor contrast between non-uniformities and surrounding regions in the disk.

Transducers used were broadband 10-MHz longitudinal wave, 5-MHz shear wave, 50-MHz longitudinal wave, and 125-MHz longitudinal wave with the megahertz value denoting the nominal center frequency. The 10-MHz longitudinal and 5-MHz shear- wave transducers consisted of a critically damped lead metaniobate crystal with an active diameter of 0.6 cm bonded to a polystyrene buffer rod 0.6 cm in diameter and 0.8 cm in length. A thin (0.04 cm) pliable polymer material attached to the buffer rod allowed ultrasound to be transmitted into the sample without the need for liquid coupling (Ultran, Boalsburg, PA). The 50- and 125-MHz longitudinal wave transducers consisted of a lead metaniobate crystal with an active diameter of 0.3 cm bonded to a silica glass buffer rod 0.6 cm in diameter and 0.8 cm in length (Panametrics, Waltham, MA). Liquid couplant (diffusion pump fluid, 704 type, Dow Corning, Midland, MI) was necessary between the transducer probe and the sample to allow ultrasonic transmission. Contamination from the couplant was assumed to be minimal because of the high average density (>98 percent) of the samples. Pulser receivers of 0.01 to 10 MHz and 1- to 150-MHz bandwidth were used with the 5- and 10-MHz and 50- and 125-MHz transducers, respectively. Signal-to-noise ratios were high (~250) for the wet-coupled configuration and moderate to low (~10 to 50) for the dry-coupled configuration.

4.3 Further Characterization

Ultrasonic immersion C-scans.—Immersion (water) C-scans were obtained by using 10- and 35-MHz focused transducers to qualitatively examine the uniformity of the Si_3N_4 disk samples and to compare them with contact scan images of the samples. Data were acquired every 100 μm in both the x- and y-directions. Transmission amplitude images were obtained by gating front and back surface reflections, and transmitted pulses were obtained by using pulse-echo and through-transmission techniques, respectively. Scans were run with the polished faces facing the sending transducer. The images show the amplitude of ultrasonic transmission in terms of gray scale with lighter gray scale corresponding to higher ultrasonic transmission. Images were contrast expanded for optimum viewing of nonuniformity.

X-ray radiography.–Microfocus radiography was used to qualitatively examine the uniformity of the disk samples and to compare them with contact scan images of the samples. Radiographs were made through the thickness of the disks with conventional contact methods under conditions optimized to yield high accuracy and contrast. The source-to-disk distance was approximately 18 in., and the exposure conditions were 35 kV, 10 mA, and 4 min. The print images show x-ray attenuation in terms of gray scale, with lighter gray scale corresponding to lower attenuation (greater porosity).

Thermal wave imaging.–Thermal wave imaging was used to determine if thermal behavior variations correlated with pore fraction variations that had been characterized metallographically and in ultrasonic images of disk SN6. The polished surface of disk SN6 was coated with a high-emissivity material to allow maximum absorption of thermal radiation into the sample. Four flashlamps were located at 45° angles to, and 18 in. away from, the polished surface. The lamps were used to externally heat SN6. Each flashlamp's power was 1.5 kJ. A high-resolution infrared camera was located in front of the disk on the same side as the flash lamps, and data were obtained at a rate of 20 frames per second. The images show thermal energy density (temperature) in terms of gray scale, with lighter gray scale corresponding to higher thermal energy density (temperature).

Microhardness measurements.–Vickers microhardness measurements were used to determine if hardness variations correlated with pore fraction variations that had been characterized metallographically and in ultrasonic images of disk SN3. Microhardness measurements were performed at the regions of high pore fraction and at surrounding regions of average pore fraction in a polished cross section of SN3. Measurements were made at a 500-g load for 15-sec duration. Twenty measurements were made at the high-pore-fraction and surrounding regions. The error in the microhardness measurement was estimated at 10percent from repeated trials.

5.0 Results and Discussion

The following sections show representative images from the contact-scanned Si_3N_4 disks. Reflection coefficient, attenuation coefficient, phase velocity, and cross-correlation velocity images obtained from contact scanning are designated as $R(f)$, $\alpha(f)$, $V_p(f)$, and V_{pulse} images, respectively.

5.1 Ultrasonic Contact Scan Images and Properties Versus Frequency

Figures 10 to 13 show $R(f)$, $\alpha(f)$, $V_p(f)$, and V_{pulse} images and mean values at 30 to 110 MHz in 10-MHz increments for disk SN2 containing six distinct regions of high pore fraction. (Nominal center frequency was 50 MHz for the transducer

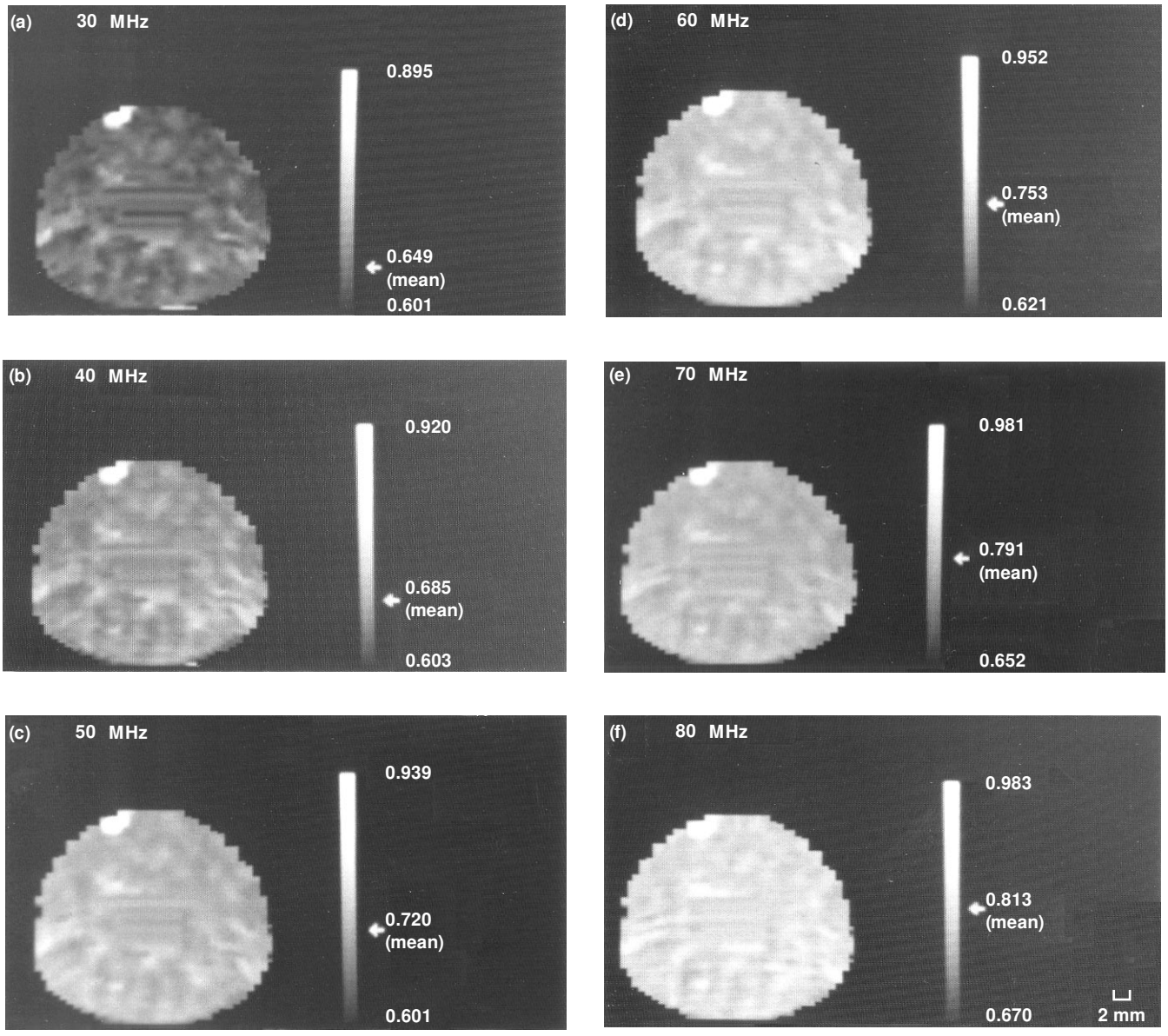

Figure 10.—Frequency-dependent reflection coefficient images and mean values at 30 to 110 MHz in increments of 10 MHz for disk SN2 containing six distinct regions of high pore fraction. (Nominal center frequency was 50 MHz for the transducer used to scan SN2.)

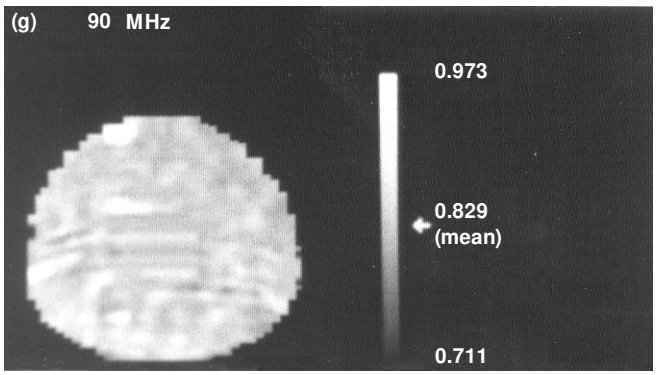

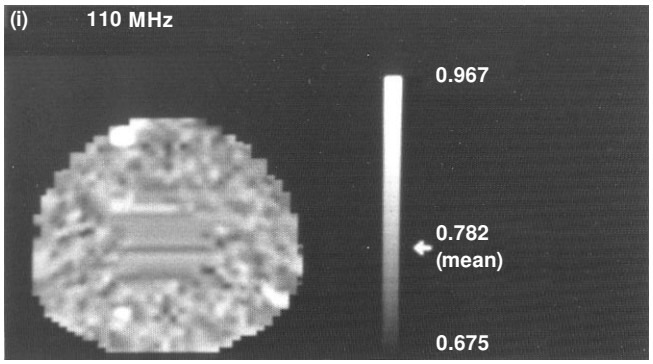

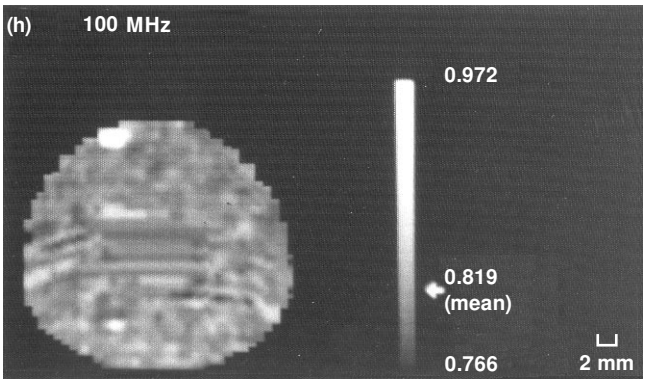

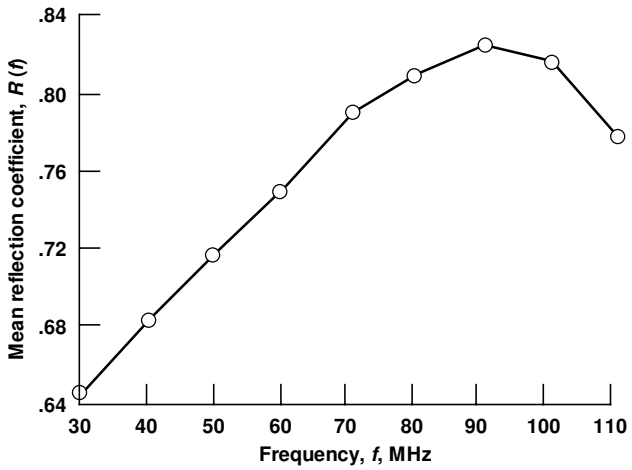

(j) Mean reflection coefficient versus frequency.

Figure 10.—Concluded.

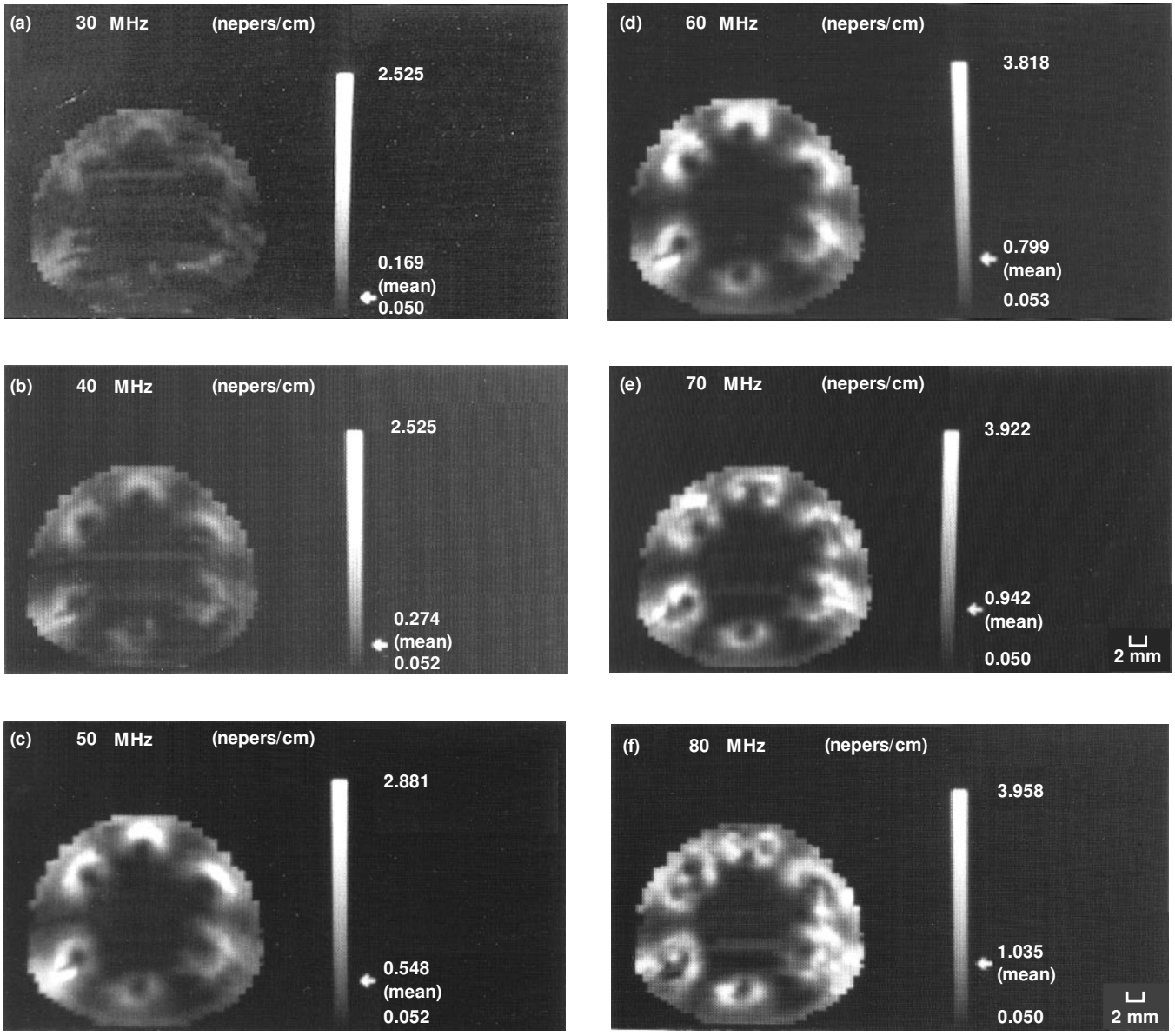

Figure 11.—Frequency-dependent attenuation coefficient images and mean values at 30 to 110 MHz in increments of 10 MHz for disk SN2 containing six distinct regions of high pore fraction. (Nominal center frequency was 50 MHz for the transducer used to scan SN2.)

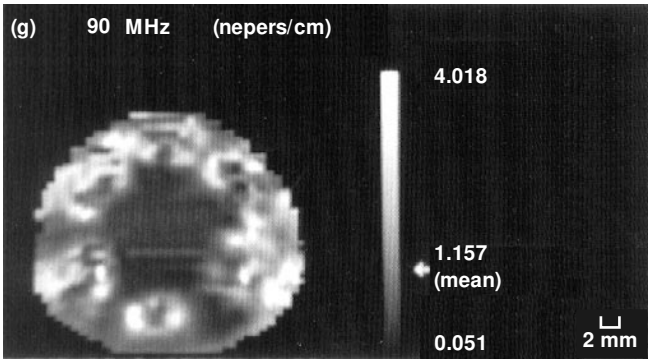

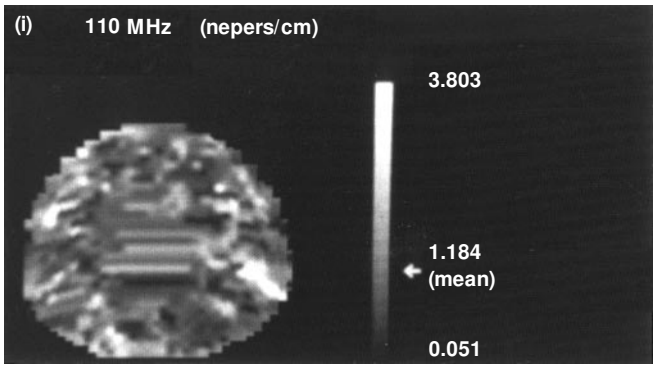

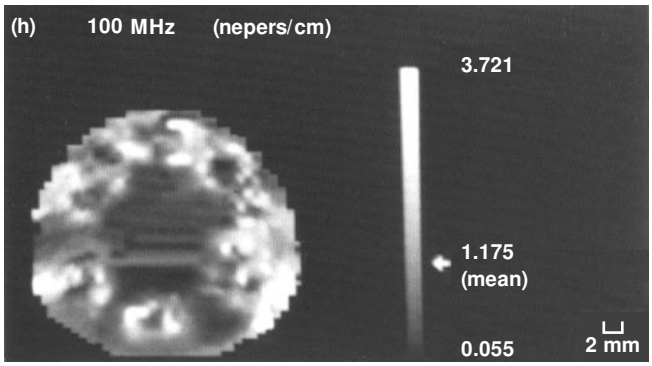

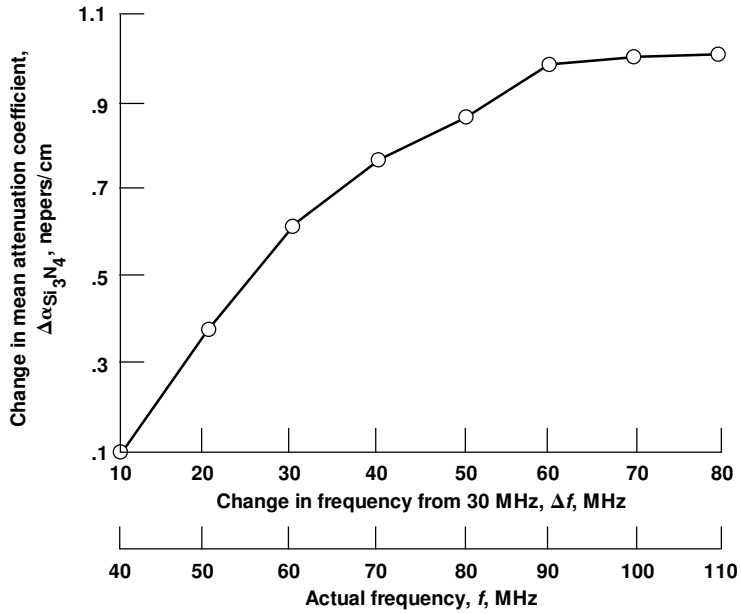

(k) Observed changes in mean $\alpha_{Si_3N_4}$ versus changes in frequency from 30 MHz.

Figure 11.—Concluded.

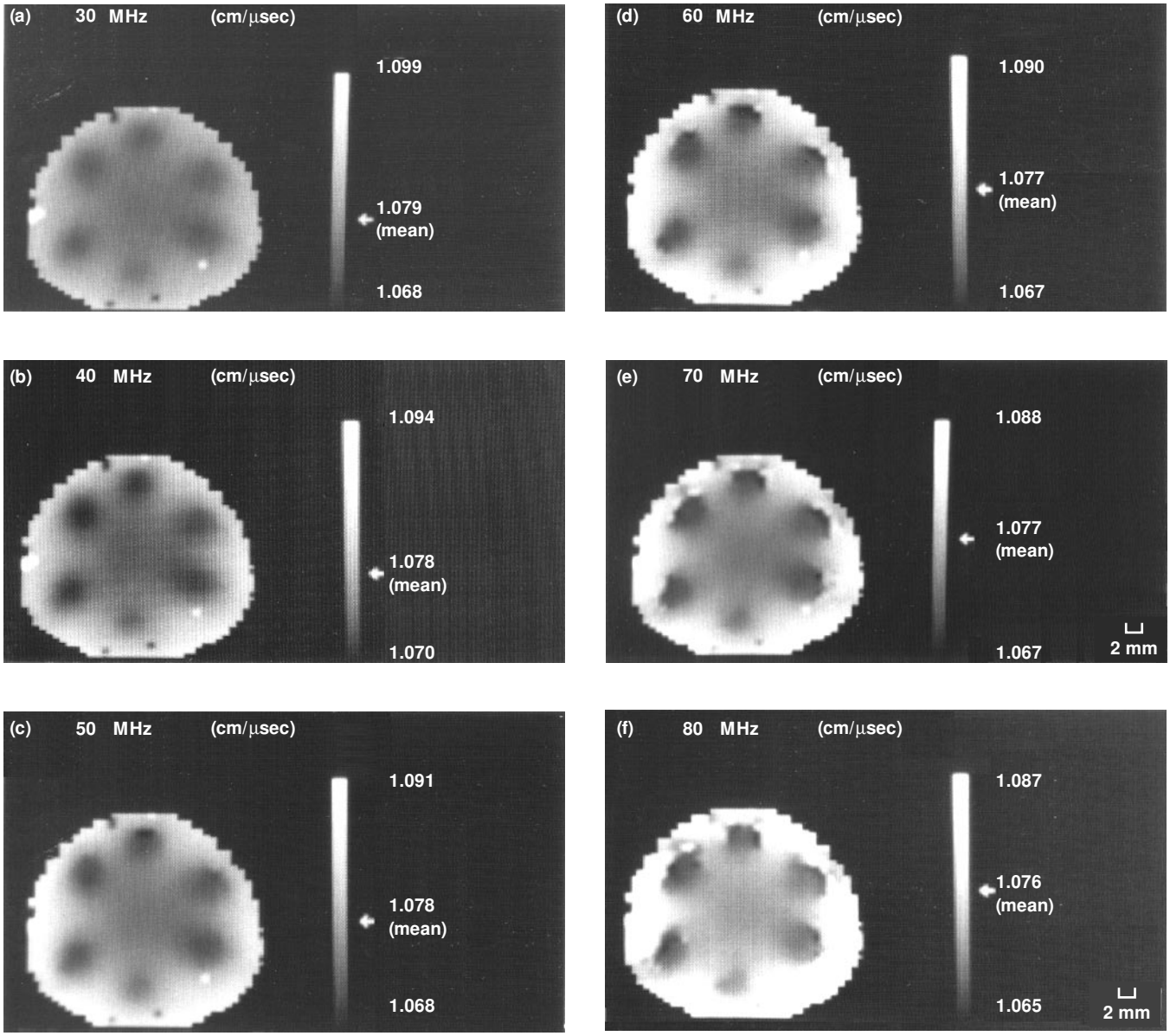

Figure 12.—Frequency-dependent phase velocity images and mean values at 30 to 110 MHz in increments of 10 MHz for disk SN2 containing six distinct regions of high pore fraction. (Nominal center frequency was 50 MHz for the transducer used to scan SN2).

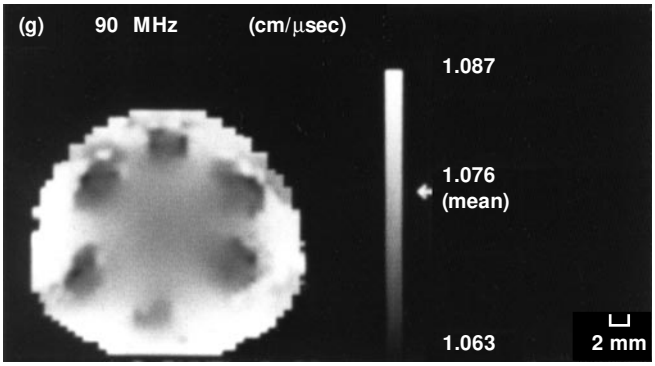

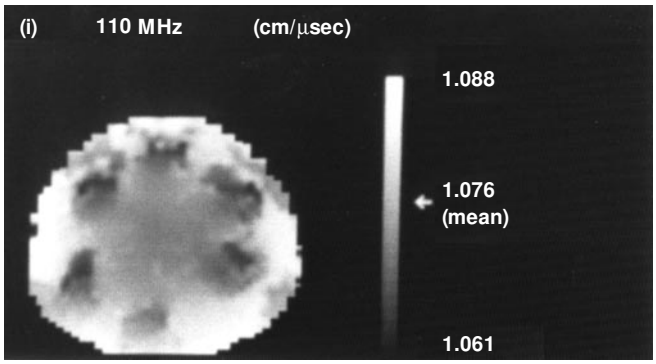

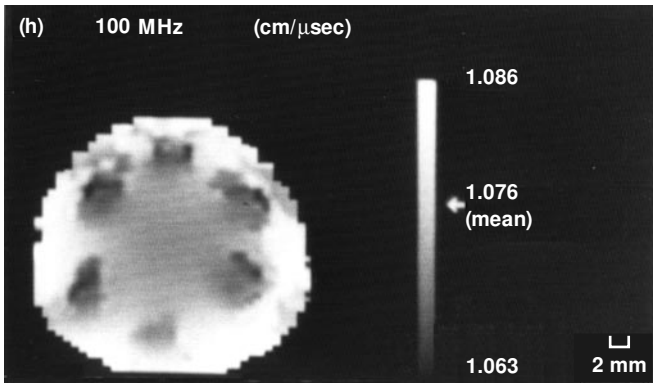

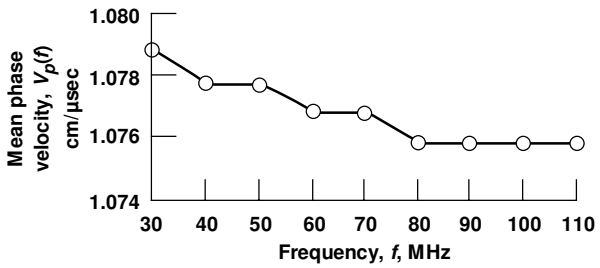

(j) Mean phase velocity versus frequency.

Figure 12.—Concluded.

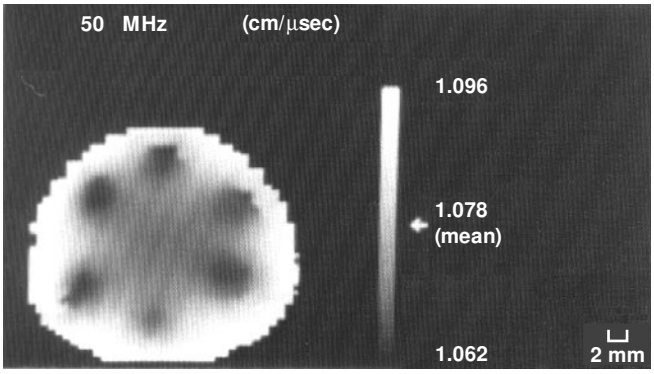

Figure 13.—Cross-correlation pulse velocity image for disk SN2 containing six distinct regions of high pore fraction. (Nominal center frequency was 50 MHz for the transducer used to scan SN2.)

used to scan SN2.) At most frequencies, $\alpha(f)$, $V_p(f)$, and V_{pulse} images clearly revealed all six regions of high pore fraction. Additionally, V_{pulse} and $V_p(f)$ images revealed pore fraction variation between the disk central section and edge regions. All image types were more "focused" toward the middle of the frequency band (50 to 80 MHz) and less focused at the frequency band extremes (≤50 MHz and ≥80 MHz). (The latter statement is not applicable to V_{pulse} images, which are formed using the whole pulse containing the broad band of frequencies.) This result is consistent with the fact that as the frequency approaches (from the peak frequency) the −6-dB frequencies (50 percent bandwidth) of the front-surface, pulse-echo magnitude spectrum (~40 and 90 MHz), the signal-to-noise ratio becomes low enough to make the results of questionable validity and is responsible for the erratic behavior of the ultrasonic properties at the frequency extremes (e.g., the decrease in mean $R_{Si_3N_4}$ above 90 MHz). Between 50 and 80 MHz, the spatial patterns of the images did not change significantly. The $R(f)$ images did not reveal the six distinct regions at any frequency. Mean values for $R(f)$ showed an approximately linear increase with increasing frequency (from 30 to 90 MHz) and ranged from 0.65 to 0.83 (fig. 10(j)). Mean values for $\alpha(f)$ increased with increasing frequency and ranged from about 0.2 to 1.2 nepers/cm (fig. 11(j)). Figure 11(k) shows changes in mean $\alpha_{Si_3N_4}$ ($\Delta\alpha_{Si_3N_4}$) versus changes in frequency Δf from 30 MHz as a means for comparison with figure 4 and will be discussed in section 5.8. Mean values for $V_p(f)$ decreased slightly (0.3 percent) with increasing frequency (fig. 12(j)) indicating this Si_3N_4 to be slightly dispersive.

5.2. Comparison of Contact Scan Results With Those From Other Techniques

Figure 14 compares imaging results from ultrasonic C-scans and microfocus radiography of disk SN6 with $\alpha(f = 70$ MHz),

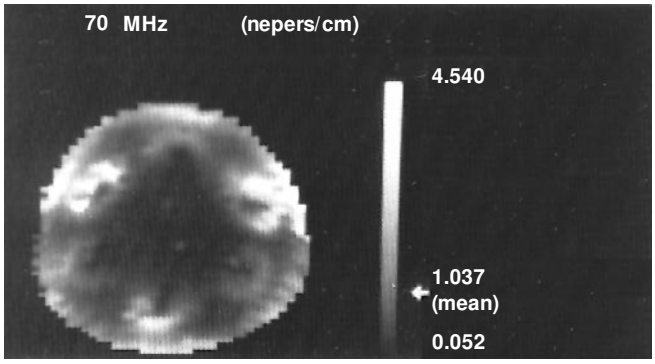

(a) $\alpha(f = 70$ MHz) image.

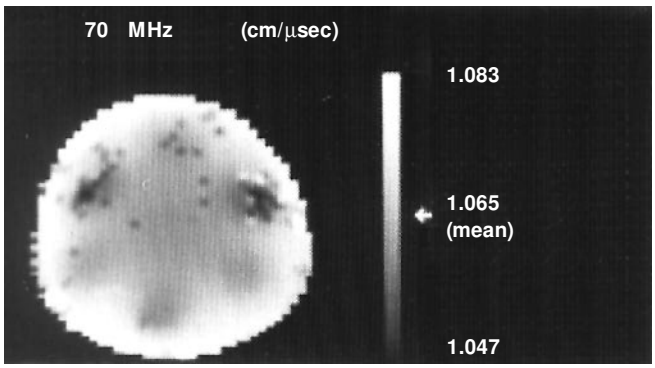

(b) V_p ($f = 70$ MHz).

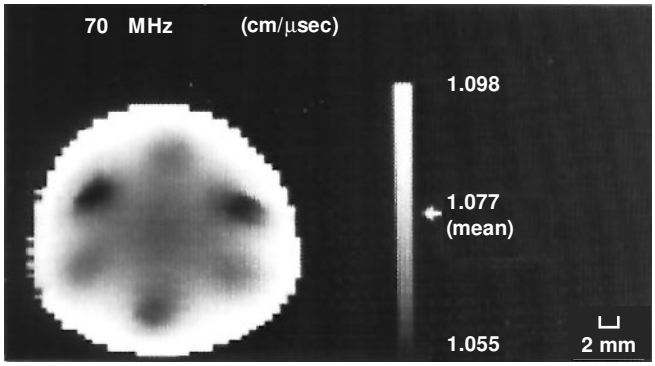

(c) V_{pulse} image; nominal center frequency, 50 MHz.

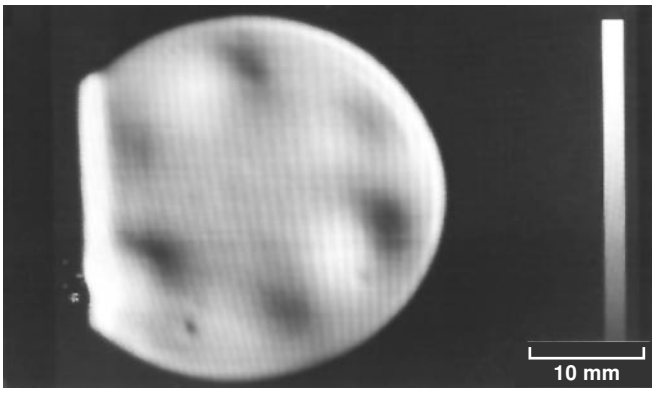

(d) Back-surface echo C-scan (10 MHz focused).

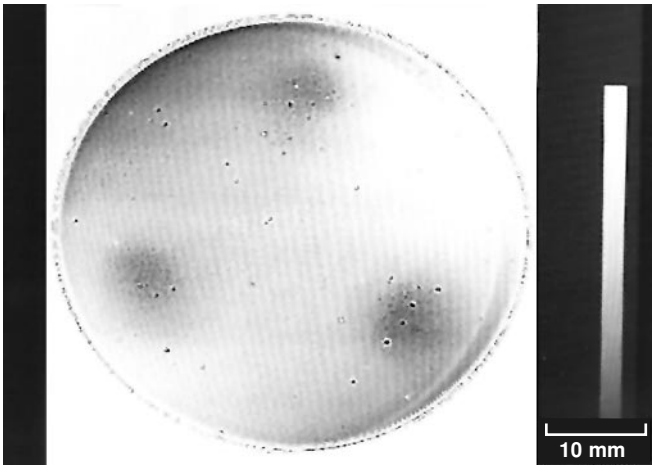

(e) Surface reflection C-scan (35 MHz focused).

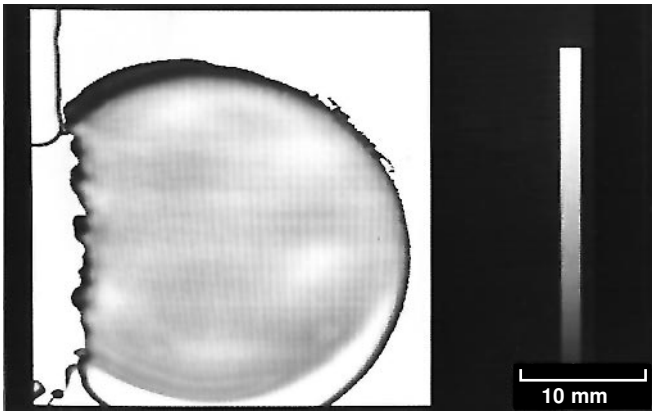

(f) Through-transmission C-scan (10 MHz focused).

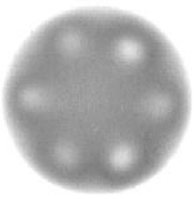

(g) Through-transmission microfocus radiograph.

Figure 14.—Comparison of conventional imaging methods with ultrasonic contact scan results.

$V_p(f = 70$ MHz), and V_{pulse} images. First, consider the conventional NDE imaging methods. C-scan back-surface echo reflection images at 10 MHz (fig. 14(d)) revealed all six distinct regions as dark (low ultrasonic transmission) areas. C-scan through-transmission images at 10 MHz (fig. 14(f)) did not reveal the regions. C-scan surface-wave images at 35 MHz (fig.14(e)) clearly revealed the three front-surface-connected regions of high pore fraction as dark (low ultrasonic transmission) areas. Microfocus x-radiography (fig. 14(g)) clearly showed all six distinct regions. Additionally, dark rings appeared to surround and highlight the porous regions in the microfocus x-ray image. Neither C-scan nor microfocus x-ray images discriminated the more porous central section from the highly dense edge region.

Consider the images obtained from contact scans. The V_{pulse} images (fig. 14(c)) quantified variation from edge to center including the variation between the distinct regions of high pore fraction and the surrounding central region (~1-percent velocity difference), the variation between the distinct regions of high pore fraction and the dense edge region (~4-percent difference), and the variation between the more porous central section and the dense edge region (~3-percent difference). (The percentage change was obtained by dividing the velocity values by the velocity expected for a fully dense Si_3N_4 sample (i.e., the theoretical velocity of 1.12 cm/μsec) (ref. 14)). *The magnitude and direction of these variations in the V_{pulse} image are similar to those seen for volumetric pore fraction variations in disk SN2 (fig. 7(b))*. The $V_p(f)$ images quantified variation over a broad band of frequencies in a similar manner to that observed in the cross-correlation velocity images. However, in some instances, $V_p(f)$ images showed more "scatter" (fig. 14(b)) (note darker-colored dots randomly located), and the variation was not quite as obvious as it was in the V_{pulse} images. The scatter could not be filtered without losing essential image features. The magnitude of velocity variation was usually similar in V_{pulse} and $V_p(f)$ images; however, minimum, maximum, and mean values varied slightly depending on the frequency of the $V_p(f)$ images and were slightly different from those observed for V_{pulse} images (e.g., mean $V_p(f = 70$ MHz) for SN6 was 1.065 cm/μsec as compared with a mean V_{pulse} of 1.077 cm/μsec).

In the $\alpha(f)$ images obtained over a broad band of frequencies, larger attenuation coefficients were observed at the edges of the distinct regions of high pore fraction than in the surrounding regions (e.g., at 70 MHz for SN6 an attenuation coefficient of ~4.5 nepers/cm was observed at the edges of the distinct regions whereas the mean attenuation coefficient was 1.04 nepers/cm). The central section appeared to have a uniformly lower attenuation coefficient at 70 MHz than the surrounding edge area (~0.1 neper/cm as compared with 0.4 to 1.0 neper/cm).

The $R(f)$ images did not discriminate the high-pore-fraction regions from the surrounding regions in disk SN6.

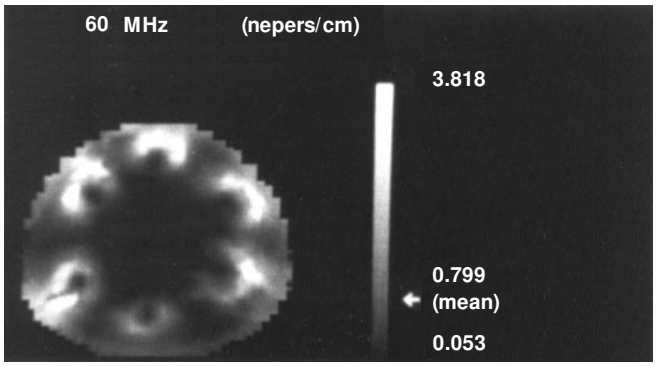

(a) SN2.

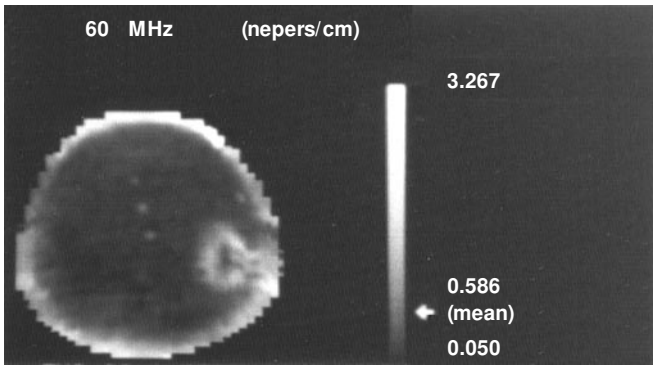

(b) SN3.

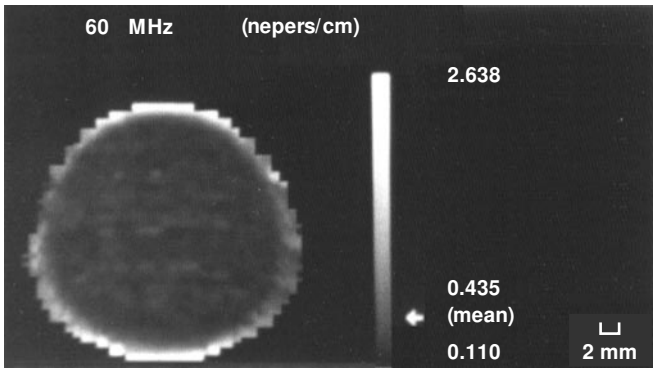

(c) SN5.

Figure 15.—α (*f* = 60 MHz) images of SN2, SN3, and SN5.

5.3 Comparison of Si_3N_4 Disks

Figures 15 to 19 show $\alpha(f = 60$ MHz and $f = 80$ MHz), $V_p(f = 60$ MHz and $f = 80$ MHz), and V_{pulse} images of the SN2, SN3, and SN5 disks. Disk SN2 contained six distinct regions of high pore fraction, disk SN3 contained one such distinct region, and disk SN5 contained no such regions; the $\alpha(f)$, $V_p(f)$, and V_{pulse} images clearly represent the differences in the disks. The more such distinct regions, the higher the mean

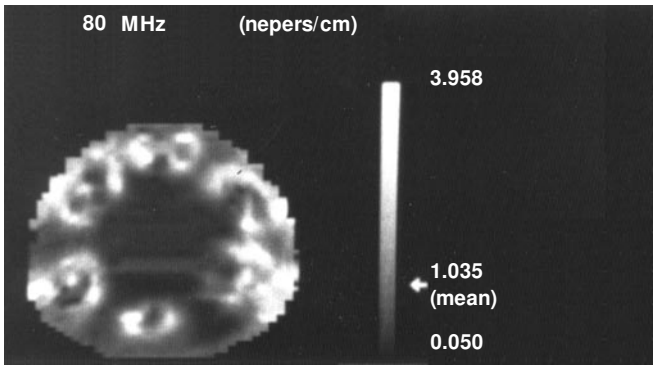

(a) SN2.

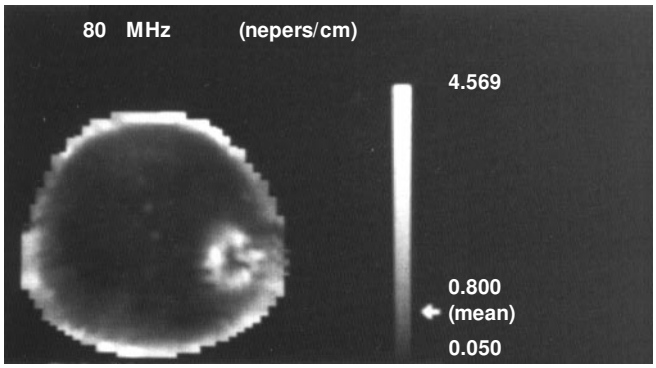

(b) SN3.

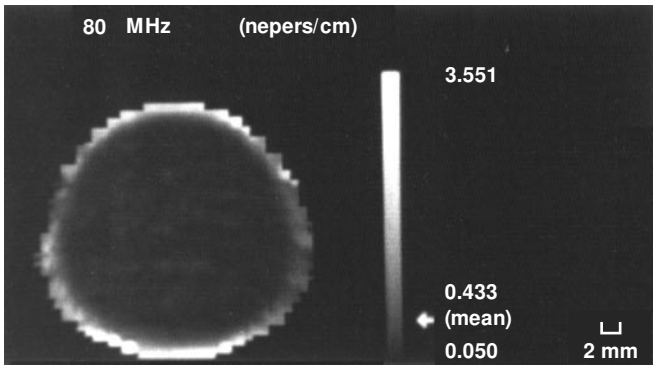

(c) SN5.

Figure 16.—α (f = 80 MHz) images of SN2, SN3, and SN5.

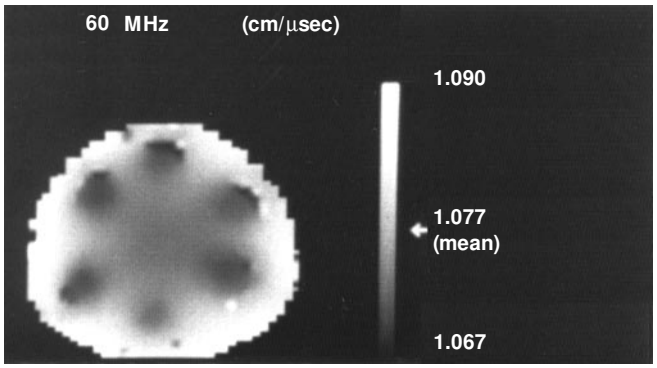

(a) SN2.

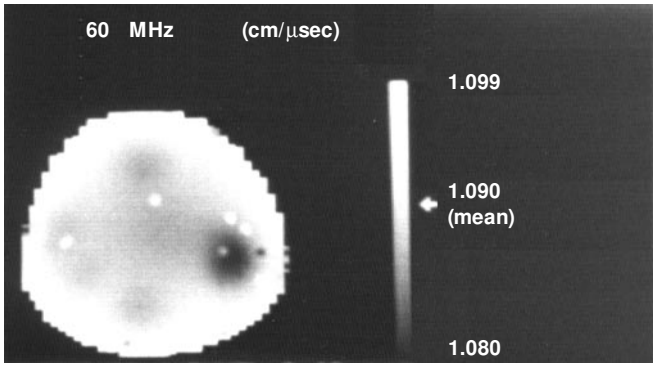

(b) SN3.

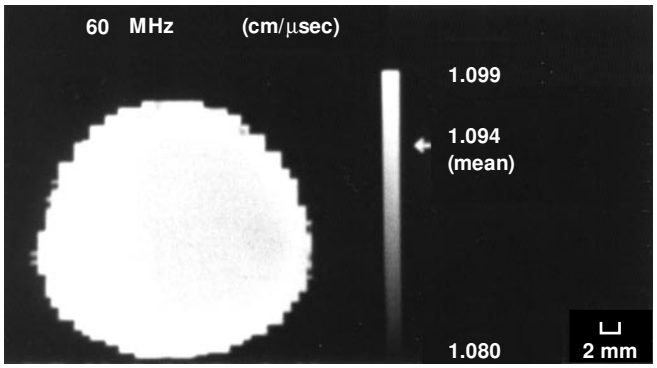

(c) SN5.

Figure 17.—V_p (f = 60 MHz) images of SN2, SN3, and SN5.

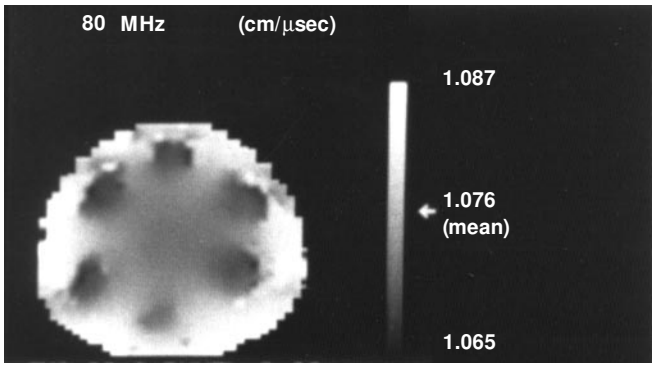

(a) SN2.

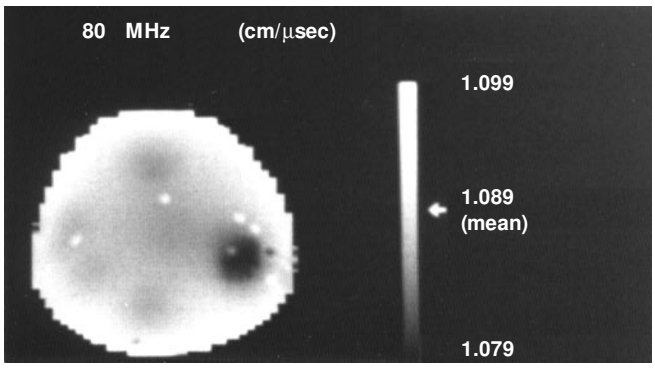

(b) SN3.

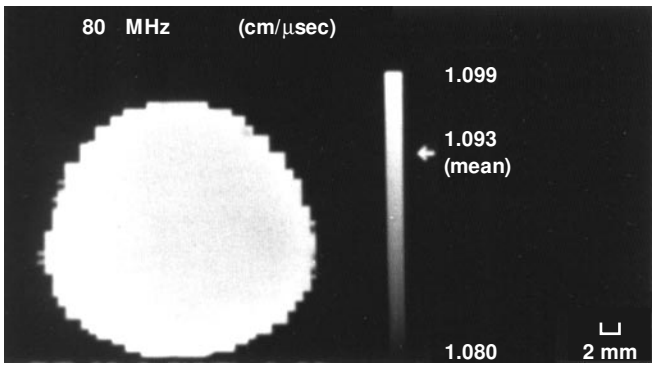

(c) SN5.

Figure 18.—V_p (f = 80 MHz) images of SN2, SN3, and SN5.

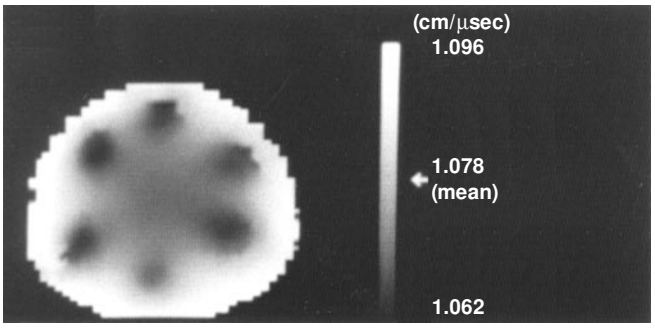

(a) SN2 (norminal center frequency, 50 MHz).

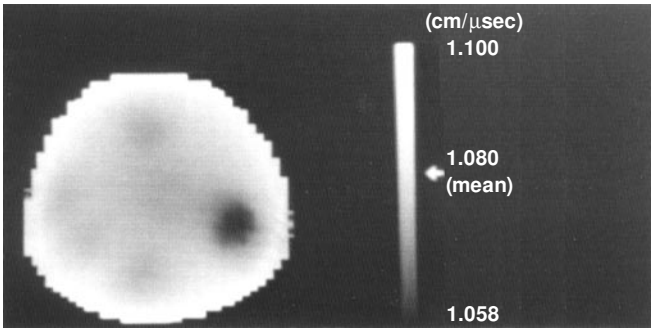

(b) SN3 (norminal center frequency, 125 MHz).

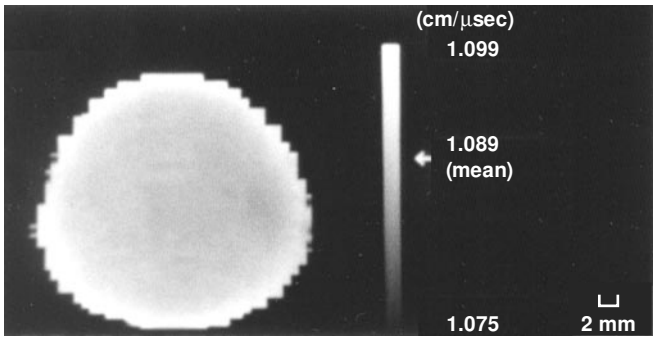

(c) SN5 (norminal center frequency, 125 MHz).

Figure 19.—V_{pulse} images of SN2, SN3, and SN5.

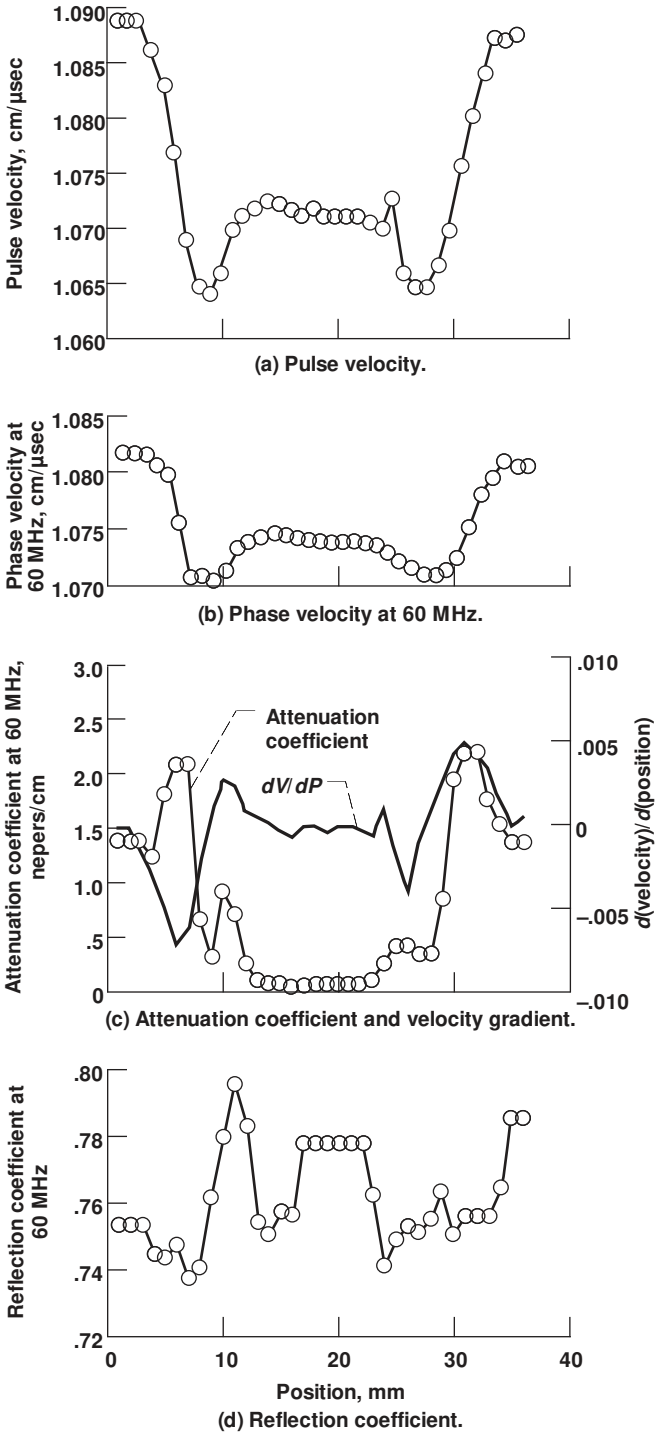

Figure 20.—Ultrasonic velocity versus position for section intercepting two high-pore-fraction regions in SN2 disk.

attenuation coefficient, and the lower the mean phase and cross-correlation velocities. The V_{pulse} images consistently were the most revealing of disk nonuniformity and differences between disks. The $R(f)$ images did not differentiate the microstructual differences between the disks.

5.4 Correlation of Ultrasonic Properties With Each Other and With Microstructure

Figures 20(a) to (c) show ultrasonic properties versus position for a section intercepting two of the high-pore-fraction regions in the SN2 disk. From first glance at $\alpha(f = 60$ MHz), $V_p(f = 60$ MHz), and V_{pulse} images of SN2 (figs. 15(a), 17(a), and 19(a), respectively), it appears that variations in velocity and attenuation coefficient correspond with each other and with the pore fraction profile shown in figure7(b). In reality, disk positions where *changes* in velocity with position *dV/dP*

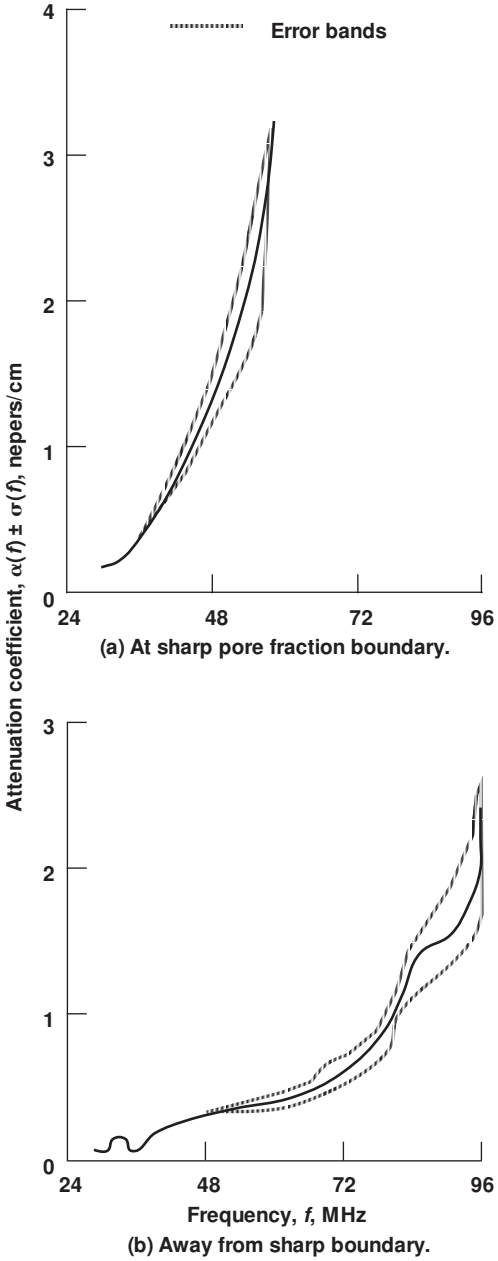

Figure 21.—α (*f*) ± σ error properties versus frequency for SN2.

were most severe corresponded to areas of highest $\alpha(f)$ (fig. 20(c)), and velocity variations corresponded exactly with pore fraction variations (compare fig. 7(b) with fig. 20(a)). Note the points on the curves in figure 20(c) at the 6- and 31-mm positions; the attenuation coefficient achieved maximums where dV/dP was most negative (at $X \sim 6$ mm) and most positive (at $X \sim 31$ mm). These results are consistent with those from a previous study (ref. 16) of ultrasonic imaging of sintered α-SiC disks. In that study, it was found that regions in $\alpha(f)$ images showing high attenuation coefficients generally overlapped boundaries seen in the corresponding V_{pulse} image (i.e., a high attenuation coefficient was observed where large spatial gradients in velocity and density existed). A plausible explanation for these results follows: It is believed that refractive scattering of waves occurs at impedance-mismatched material boundaries (see the distinction between the high-pore-fraction and surrounding regions in fig. 8). This results in an apparent attenuation coefficient being measured as ultrasonic energy is redirected. The effect on the measured attenuation coefficient is difficult to predict, since it is difficult to know exactly how the ultrasound is redirected. Thus, such refractive scattering effects may lead to both high and low values for the measured attenuation coefficient. In this study, high attenuation coefficients were observed at relatively sharp pore fraction boundaries.

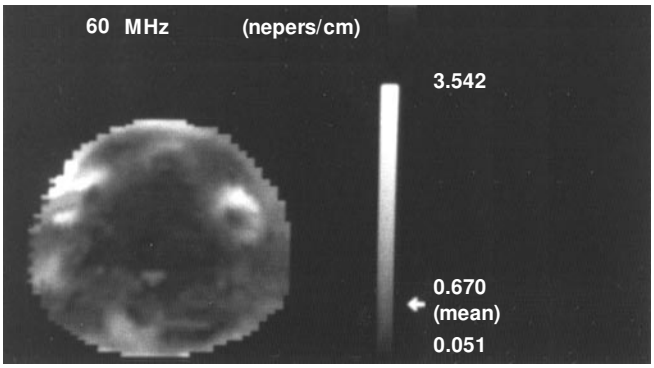

(a) Machined surface.

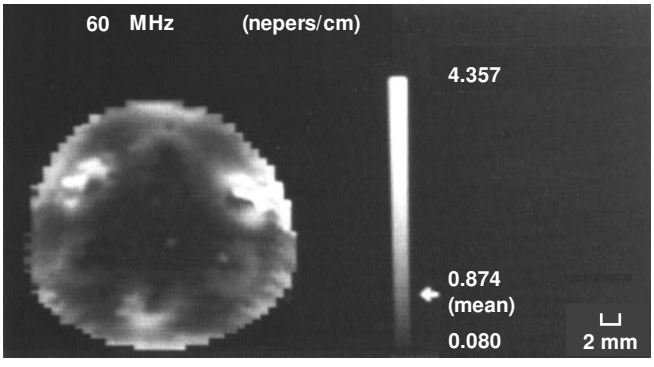

(b) Polished surface.

Figure 22.—α (f = 60 MHz) images for SN6 with transducer on machined and polished surfaces.

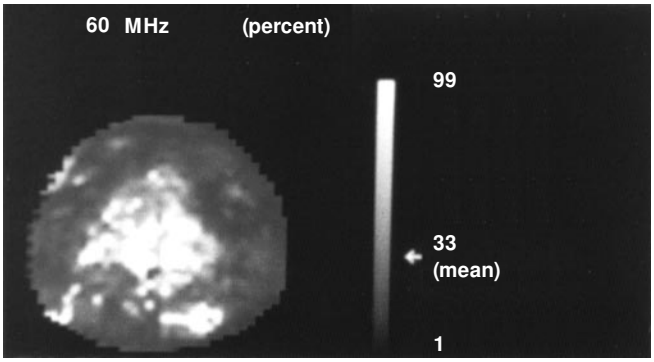

(a) Machined surface.

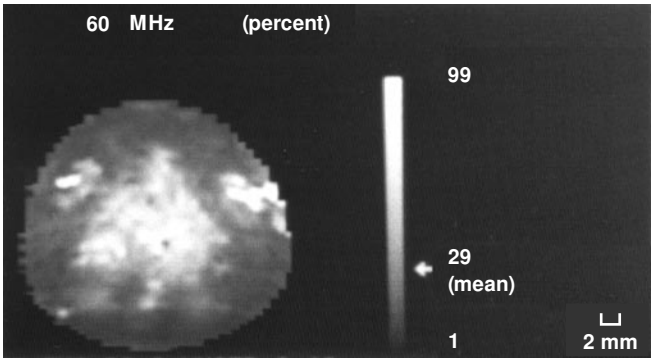

(b) Polished surface.

Figure 23.—Percent error in α (f = 60 MHz) images for SN6 with transducer on machined and polished surfaces.

It is also interesting to note that the dependence of $\alpha(f)$ on frequency was quite different at a relatively sharp pore fraction boundary than in a surrounding region in the SN2 disk (fig. 21). Therefore, the slope of $\alpha(f)$ ($d\alpha(f)/df$) may also provide information on spatial differences in microstructure (refs. 34 and 35).

The curves of pulse velocity and phase velocity are similarly shaped, but the reflection coefficient variations (fig. 20(d)) do not correspond with variations in the other curves of ultrasonic property versus position.

5.5 Comparison of Ultrasonic Contact Scan Images for Scans on Machined and Polished Disk Faces

Figures 22 to 26 show $\alpha(f = 60$ MHz) and the percent error in $\alpha(f = 60$ MHz), $V_p(f = 70$ MHz), V_{pulse}, and $R(f = 60$ MHz) images for the experimental configuration where the ultrasonic transducer was scanned first on the machined face and then on the polished face (opposite surface) for disks SN6, SN3, SN4, and SN5. In most cases, no significant differences in feature differentiation were noted between the same image types for machined and polished face scans (note that each disk

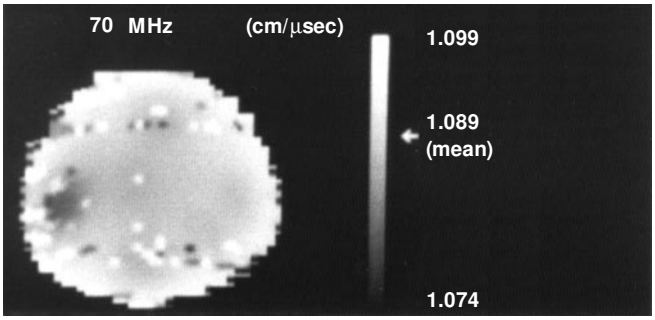

(a) Machined surface.

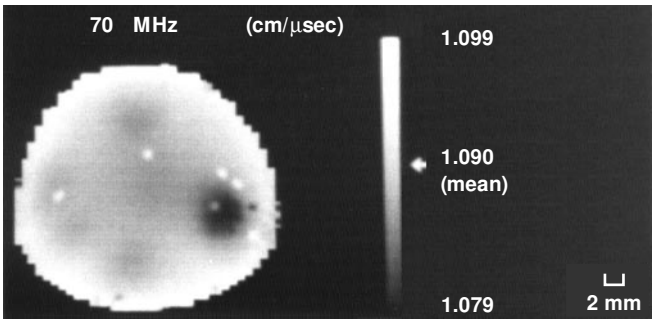

(b) Polished surface.

Figure 24.—V_p (f = 70 MHz) images for SN3 with transducer on machined and polished surfaces.

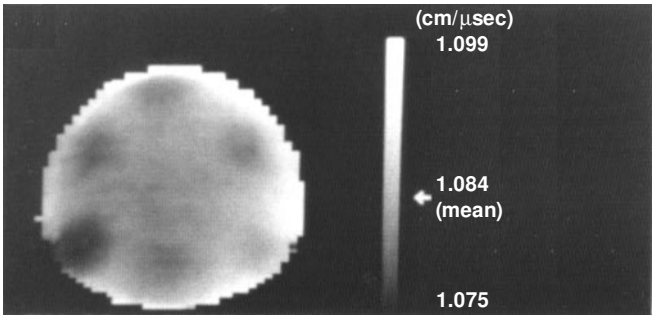

(a) Machined surface.

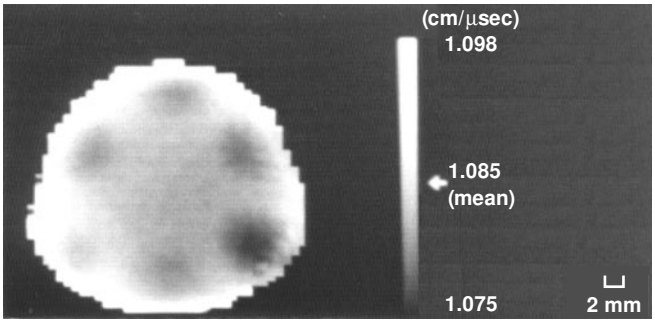

(b) Polished surface.

Figure 25.—V_{pulse} images for SN4 with transducer on machined and polished surfaces. Nominal center frequency, 125 MHz.

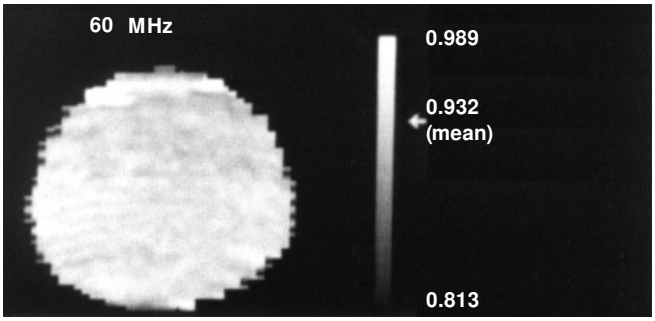

(a) Machined surface.

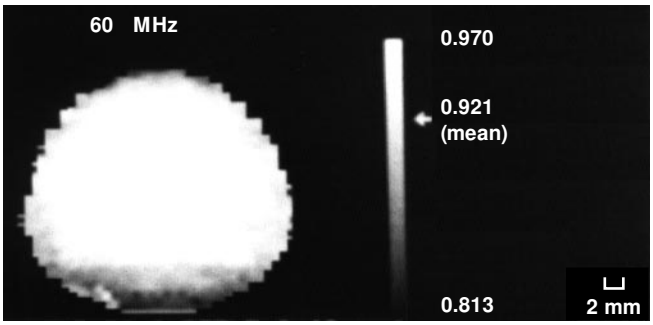

(b) Polished surface.

Figure 26.—R (f = 60 MHz) images for SN5 with transducer on machined and polished surfaces.

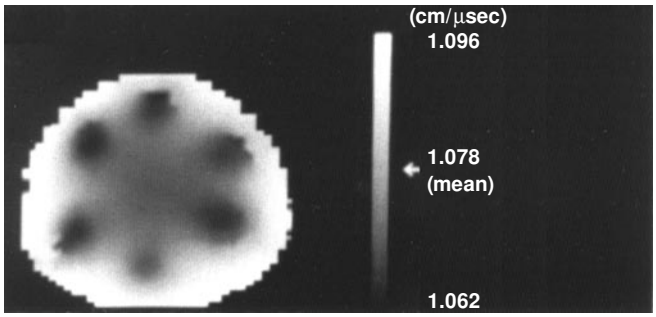

(a) Wet coupled (nominal transducer center frequency, 50 MHz; transducer diameter, 0.125 in.).

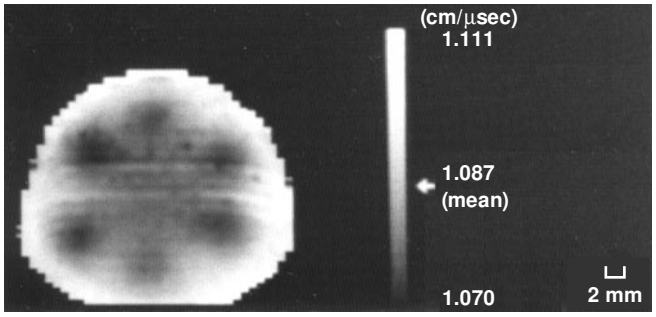

(b) Dry coupled (nominal transducer center frequency, 10 MHz; transducer diameter, 0.25 in.).

Figure 27.—V_{pulse} images of disk SN2.

was flipped over for the polished scan after scanning on the machined surface). Mean values of $\alpha(f = 60$ MHz) for SN6 from machined and polished face scans differed by about 25 percent, but this is within the mean experimental error (~30 percent) for the $\alpha(f = 60$ MHz) image (fig. 23). The minimum, maximum, and mean values for $V_p(f = 70$ MHz) images of SN3 were nearly identical for machined and polished face images. More scatter dots (discussed previously) were apparent in the machined face image than in the polished face image for $V_p(f = 70$ MHz), and it appears that slightly more detail was differentiated in the polished face image. However, the latter two results were not always observed for machined versus polished $V_p(f)$ images and are probably caused by small scan-to-scan and within-scan couplant variations. Minimum, maximum, and mean values for V_{pulse} images of SN4 were essentially identical for the machined and polished face images. Mean and maximum values for $R(f = 60$ MHz) images of SN5 were each very similar for machined and polished face images. A low reflection coefficient strip was apparent in the polished face image but not in the machined face image. The latter result was not always observed for machined versus polished $R(f)$ images and probably results from couplant thickness variations (fig. 3(c)). The results of the machined versus polished face scans were surprising considering the expected sensitivity of frequency-dependent properties on surface condition and allow the reliable application of the contact scan method to materials with machined as well as polished surfaces.

5.6 Dry- Versus Wet-coupled V_{pulse} Images

In figure 27, a wet-coupled V_{pulse} image of disk SN2 (obtained at a nominal transducer center frequency of 50 MHz and a transducer diameter of 0.125 in. (0.3 cm)) is compared with a dry-coupled V_{pulse} image (obtained at a nominal transducer center frequency of 10 MHz and a transducer diameter of 0.25 in. (0.6 cm)). Both images clearly reveal and similarly quantify the six distinct regions of high pore fraction. This result is important for materials that cannot be ultrasonically examined with wet coupling. The high-pore-fraction regions are most clearly revealed in the wet-coupled image, as is consistent with the facts that the beam diameter for the wet-coupled configuration was approximately half that for the dry-coupled configuation and that the wet-coupled configuration had approximately an order of magnitude higher signal-to-noise ratio than the dry-coupled configuration. The minimum, maximum, and mean values were uniformly about 1 percent higher in the dry-coupled image than in the wet-coupled image.

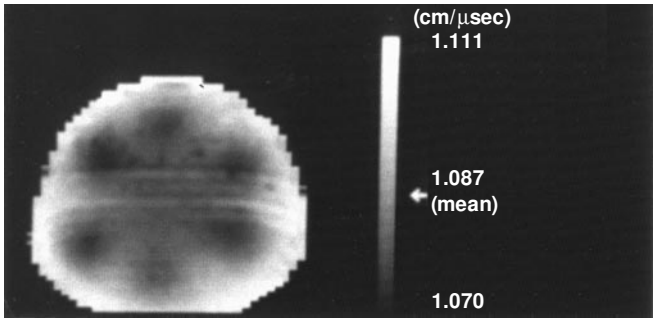

(a) V_{pulse} image from dry-coupled, longitudinal wave scan (nominal transducer center frequency, 10 MHz).

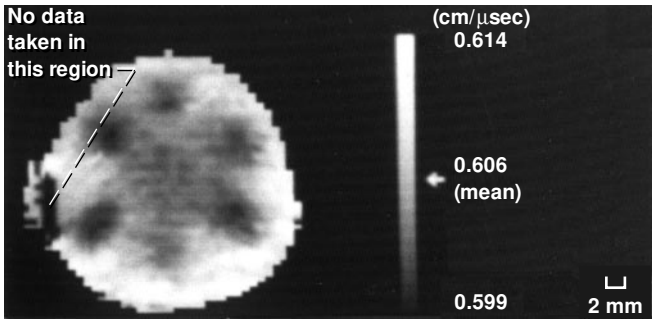

(b) V_{pulse} image from dry-coupled, shear-wave scan (nominal transducer center frequency, 5 MHz).

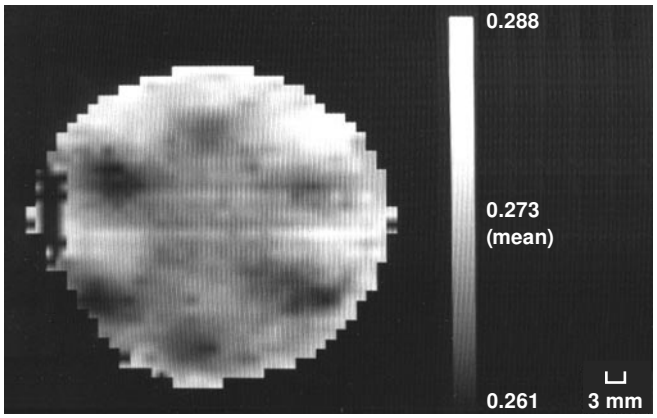

(c) "Apparent" Poisson's ratio images of same disk constructed from longitudinal and shear-wave velocity images.

Figure 28.—V_{pulse} and Poisson's ratio images of disk SN2.

5.7 Longitudinal Versus Shear-Wave V_{pulse} Images and Poisson's Ratio Maps

Figures 28(a) and (b) show ultrasonic longitudinal (nominal transducer center frequency, 10 MHz) and shear-wave (nominal transducer center frequency, 5 MHz) V_{pulse} images, respectively, of SN2 obtained from dry-coupled scans. (The relatively low signal-to-noise ratio for the shear-wave, dry-coupled configuration resulted in data not being acquired at some scan points near the left edge of the disk during the shear-wave scan.) Both images clearly reveal and similarly quantify the six distinct regions of high pore fraction. Velocity variation was about 4 percent over the longitudinal-wave V_{pulse} image and about 2 percent over the shear-wave V_{pulse} image.

Poisson's ratio ν can be computed directly from longitudinal and shear-wave velocities according to (ref. 13)

$$\nu = \frac{\frac{V_L^2}{2} - V_S^2}{V_L^2 - V_S^2} \tag{19}$$

where V_L and V_S are the longitudinal and shear-wave velocities, respectively. Predictions of mechanical and thermal behavior of components (by finite element analysis, e.g.) traditionally assume a constant value for Poisson's ratio. This assumption can lead to reduced accuracy of the analysis if in fact "apparent" Poisson's ratio (ref. 14) varies within a component because of microstructural variation. The use of materials in demanding high-performance applications where subtle within-sample mechanical property aberrations are intolerable may require characterization of such aberrations (refs. 2 and 3). Figure 28(c) shows the apparent Poisson's ratio image of the SN2 disk constructed from the longitudinal and shear-wave velocity images through the use of equation (7). The Poisson's ratio image indicates similar variations to those shown in the velocity images and quantifies variations in Poisson's ratio across the disk. Apparent Poisson's ratio varied across the disk from ~0.26 to 0.29 (~10-percent variation) with a mean value of ~0.27. The relative error in the Poisson's ratio image was ≤1 percent as the longitudinal and shear-wave V_{pulse} images used to form the Poisson's ratio image were reproducible to 0.1 percent. The Poisson's ratio image can in concept be used in a NASTRAN finite element analysis (ref. 36) by dividing the disk into a finite element grid, using different material cards for finite elements having different Poisson's ratios, and inputting the appropriate value of apparent Poisson's ratio on each material card.

Elastic properties such as Poisson's ratio are most accurately calculated from phase velocities, since the elasticity of a material may depend on the loading rate (ref. 23). As previously mentioned, velocity determined from cross-correlation is essentially a pulse velocity, as the entire wave train (containing a broad band of frequencies) is considered in the calculation. Pulse and phase velocity will be essentially equal over the frequency bandwidth investigated if dispersion (velocity varying with frequency) due to the material itself and sample geometry are negligible. Since essentially no dispersion was apparent for this Si_3N_4 material, the Poisson's ratio values obtained from cross-correlation velocity measurements were deemed to be sufficiently accurate and are close to values obtained in other studies (ref. 37).

5.8 Experimental Versus Expected Results for Frequency and Pore Fraction Dependence

Figure 29 shows the experimental relations for ultrasonic properties versus frequency obtained for SN2 with the ultrasonic transducer placed directly at the disk center (~0.03 pore fraction averaged through the thickness), at the disk edge (~0.01 pore fraction averaged through the thickness), and in the high-pore-fraction regions (~0.04 pore fraction averaged through the thickness) (fig. 7(b)). The following comments pertain to the frequency range of approximately 30 to 110 MHz. Below and above this frequency range, the low signal-to-noise ratio produced results of questionable validity as previously explained (section 5.1).

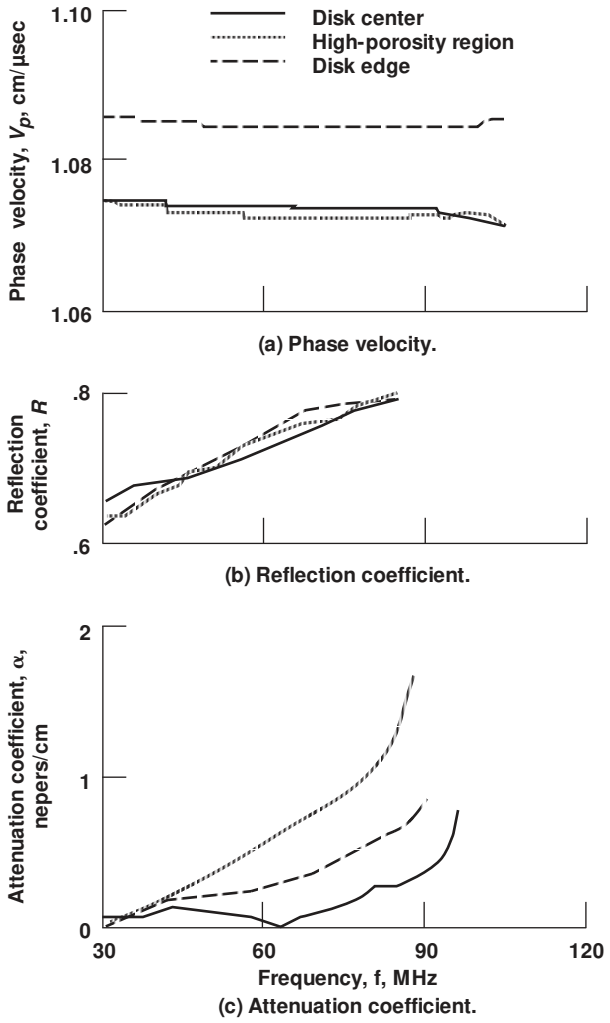

Figure 29.—Experimental relations for ultrasonic properties versus frequency obtained for SN2 directly at disk center (~0.03 pore fraction averaged through thickness), disk edge (~0.01 pore fraction averaged through thickness), and high-pore-fraction regions (~0.04 pore fraction averaged through thickness).

Phase velocity $V_{Si_3N_4}$ decreased with increasing pore fraction at any frequency and decreased slightly with increasing frequency (fig. 29(a)). These results agree well with those predicted (fig. 2(c)). Absolute magnitudes of velocity values and magnitudes of changes in velocity values with changing pore fraction correlated with predicted theoretical (fig. 2(a)) and previously observed empirical (fig. 2(b)) results.

The reflection coefficient $R_{Si_3N_4}$ had no predictable dependence on pore fraction and increased with increasing frequency

for all pore fractions (fig. 29(b)). Regarding the latter result, experimental results agreed with those predicted. The $R_{Si_3N_4}$ was expected to slightly decrease with increasing pore fraction (fig. 3(a)); experimental results showing no pore fraction dependence for $R_{Si_3N_4}$ were surprising, since the regions of high pore fraction were readily apparent at disk surfaces (fig. 5). The behavior of $R_{Si_3N_4}$ versus frequency appears to indicate a couplant thickness of ~0.5 μm (fig. 3(c)). Comparing the reflection coefficient for Si_3N_4 calculated from velocities and densities ($R_{Si_3N_4}$ = 0.46) (ref. 13) with the larger frequency-dependent $R_{Si_3N_4}$ observed experimentally revealed the necessity of using the experimentally observed reflection coefficient to determine accurate attenuation coefficients.

Attenuation coefficient $\alpha_{Si_3N_4}$ increased with increasing frequency for all pore fractions (fig. 29(c)). The increases were on the order of ≤1 neper/cm over the frequency range 30 to 110 MHz. The $\alpha_{Si_3N_4}$ versus frequency behavior at distinctly different pore fraction regions was not *consistently* different. A variation was expected, since grain size distribution did not appear to vary between the high-pore-fraction and surrounding regions. However, it is difficult to make conclusive statements regarding the effects of pore fraction changes on changes in $\alpha_{Si_3N_4}$ by using the methodology of this study. Apparent attenuation coefficient may have been measured and imaged because of scattering at relatively sharp material boundaries as discussed previously (the dependences of $\alpha(f)$ on frequency, and the values for $\alpha_{Si_3N_4}$ were observed to be significantly different between pore fraction *boundaries* and regions away from such boundaries as shown in fig. 21). Further competing material effects (such as second-phase variations) may have

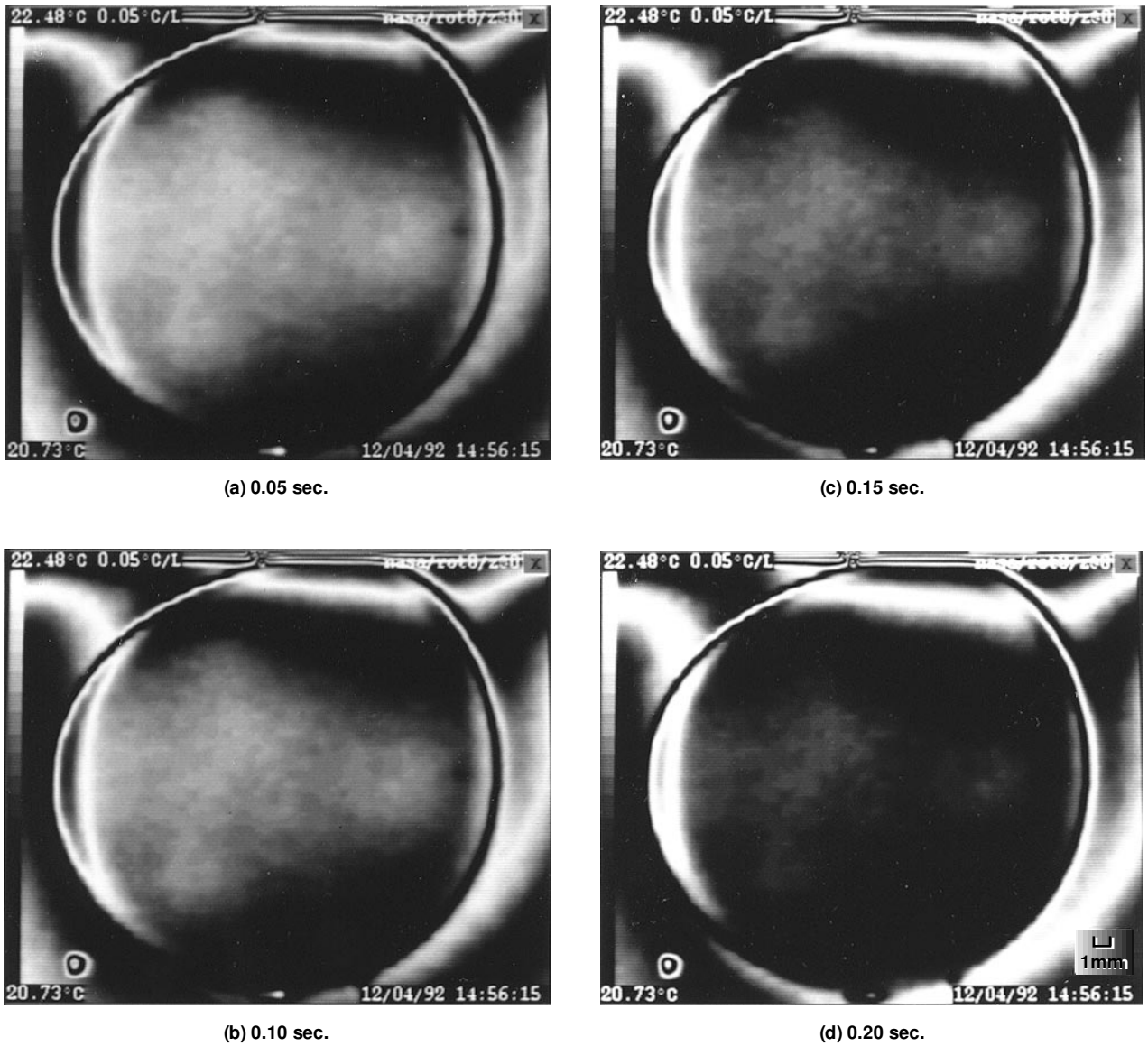

(a) 0.05 sec.

(c) 0.15 sec.

(b) 0.10 sec.

(d) 0.20 sec.

Figure 30.—Thermal wave images of disk SN6.

also been present and affecting $\alpha_{Si_3N_4}$. Expected changes in $\alpha_{Si_3N_4}$ due to scattering from pores (fig. 4(c)) were compared with observed changes in mean $\alpha_{Si_3N_4}$ with changes in frequency (fig. 11(k)). An average pore concentration n_o of approximately $10^8/cm^3$ was indicated by the observed magnitude of change (≤1 nepers/cm from 30 to 110 MHz) (if grain scattering and other contributions to $\alpha_{Si_3N_4}$ were assumed to be negligible and pores were approximately 1-μm radius).

5.9 Correlation of Ultrasonic Contact Scan Results With Physical Properties

Hardness.—The average of 20 Vickers microhardness measurements in each region yielded similar apparent Vickers hardness numbers (mean ± standard deviation) of 1126 ± 56 for the high-pore-fraction region and 1103 ± 58 for the surrounding less porous regions of disk SN3. Thus, Vickers microhardness measurements were not able to clearly discriminate the pore fraction variation.

Thermal behavior.—Thermal behavior variations correlated with pore fraction variations in disk SN6 as shown in four successive time frames separated by 0.05 sec in figure 30. The three front-surface-connected regions of high pore fraction, as well as the generally less dense central section of disk SN6, were highlighted by lighter gray scale (higher thermal energy density). Variations were most prominent in frames 1 and 2 and began to fade out later in time. The initial magnitude of variation between highly porous and surrounding regions was on the order of 2 deg C. (None of the the six distinct regions of high pore fraction were differentiated in thermal diffusivity images when using a similar procedure. Average thermal diffusivity was 0.23±0.03 cm^2/sec for disk SN6, which agreed well with those previously reported (0.22 to 0.26 cm^2/sec) for sintered Si_3N_4 (ref. 38).)

6.0 Further Discussion

The potential of the ultrasonic contact scan technique for materials characterization was demonstrated in this study. A single transducer in combination with spectral analysis allowed material characterization in terms of ultrasonic material properties over a wide band of frequencies. This method results in time savings over scanning using discrete frequency techniques. The ultrasonic contact scan technique is applicable to flat machined materials in which access to only one side is possible and is most useful in a materials development program for quantitative characterization of sample homogeneity. It is also envisioned that this method would be useful in a quality assurance laboratory for material coupon analysis. The scan system hardware and software can be upgraded for improvements or additions with the following envisioned: First, with the development of wheel probes and multielement assemblies for scanning (ref. 39), and the ever-increasing power of computers for data acquisition and analysis, scan and analysis time can be significantly reduced in the future. Second, images of additional ultrasonic properties, such as group velocity, peak frequency of the material-modulated ultrasonic echo, and attenuation coefficient slope, can be constructed by using the digitized and stored ultrasonic waveform data. These properties and images can be used for further analysis and verification of microstructural condition.

7.0 Conclusions

An ultrasonic scan procedure using the pulse-echo contact configuration was employed to obtain maps of pore fraction variations in polished and machined sintered silicon nitride samples in terms of ultrasonic material properties. Ultrasonic velocity (pulse and phase), attenuation coefficient, and reflection coefficient images were obtained simultaneously over a broad band of frequencies (e.g., 30 to 110 MHz) by using spectroscopic analysis. Wet and membrane (dry) coupling techniques and longitudinal and shear-wave energies were used. The essential features of this study were as follows:

1. Velocity and attenuation coefficient images represented average through-thickness microstructure for the sample scanned. Ultrasonic velocity (longitudinal and shear wave) images revealed and quantified the extent of pore fraction variation in the silicon nitride disks. The magnitude and direction of variations in cross-correlation velocity images were very similar to those seen for pore fraction variations. Velocity images were similar for wet and membrane coupling. Attenuation coefficient images revealed pore fraction nonuniformity due to the scattering that occurred at boundaries between regions of high and low pore fraction. The contact scan procedure proved more precise and accurate (i.e., more quantitative) than ultrasonic C-scans by characterizing inhomogeneity in terms of ultrasonic material properties. Spatial patterns of velocity and attenuation coefficient images from a contact scan were nearly identical at frequencies within the 50-percent bandwidth (50 to 80 MHz) but became unfocused at frequency extremes. Mean, minimum, and maximum values of reflection coefficient and attenuation coefficient significantly varied with frequency throughout the entire bandwidth, but values for phase velocity varied only slightly with frequency.

2. Velocity and attenuation coefficient images were nearly identical for machined and polished disks, making the method readily applicable to flat machined materials.

3. Maps of "apparent" Poisson's ratio constructed from longitudinal and shear-wave velocities quantified Poisson ratio variations across a silicon nitride disk. A direct application of engineering ultrasonics is shown, since the Poisson's ratio map with its grid of values can be input to a finite element problem where ideal properties were previously assumed.

4. Experimental velocity results agreed well with those predicted as a function of pore fraction and frequency. Experimental reflection coefficient results agreed well with those predicted as a function of frequency for couplant thickness of approximately 0.5 μm but did not show the expected dependence on pore fraction. Experimental results of attenuation coefficient changes were similar to those predicted due to pore scattering as a function of change in frequency for a pore concentration of $10^8/cm^3$.

5. Thermal wave images of a disk indicated transient thermal behavior variations consistent with observed pore fraction and velocity and attenuation coefficient variations.

Lewis Research Center
National Aeronautics and Space Administration
Cleveland, Ohio, February 3, 1993

Appendix A
Errors Associated With Pulse-Echo Measurements

The percent error in the pulse-echo velocity V measurement was calculated from (ref. 40)

$$\%\mathrm{ERR}_V = 100\left[\left(\frac{\Delta X}{X}\right)^2 + \left(\frac{\Delta\tau}{\tau}\right)^2\right]^{0.5} \tag{20}$$

where X and ΔX are thickness and error in thickness, respectively, and τ and $\Delta\tau$ are time delay and error in time delay, respectively. Figure 31 shows the percent error associated with pulse-echo velocity measurements. (Error is also dependent on the error in frequency-domain signal processing methods used in the calculation of ultrasonic properties.)

The percent error in the reflection coefficient R measurement is calculated from

$$\%\mathrm{ERR}_R = 100\frac{\left(1+R^2\right)^{0.5}}{(\mathrm{SNR})(R)} \tag{21}$$

where SNR is the signal-to-noise ratio of the first front-surface echo without the sample present on the buffer rod. It was measured by comparing the peak amplitude of $FS_1(t)$ to the peak amplitude of the noise. The SNR was ~250 in this investigation (wet coupling configuration). Figure 32 shows the percent error associated with pulse-echo reflection coefficient measurement. The error in R was low except at low values of R and SNR.

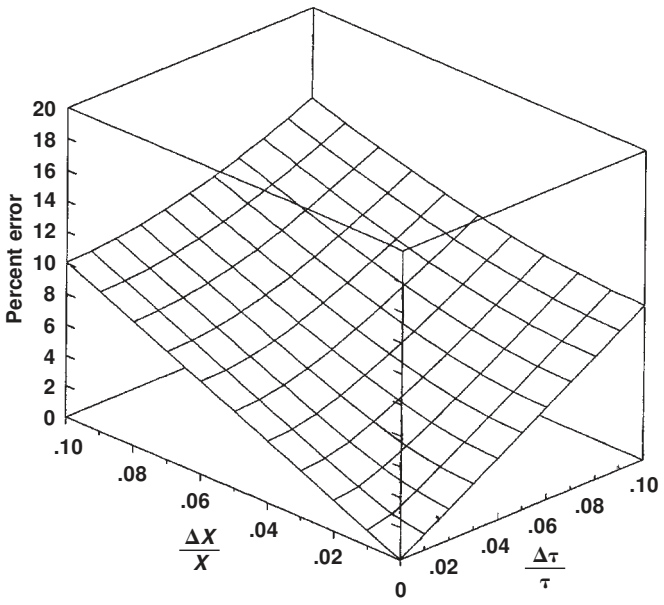

Figure 31.—Percent error associated with pulse-echo velocity measurements.

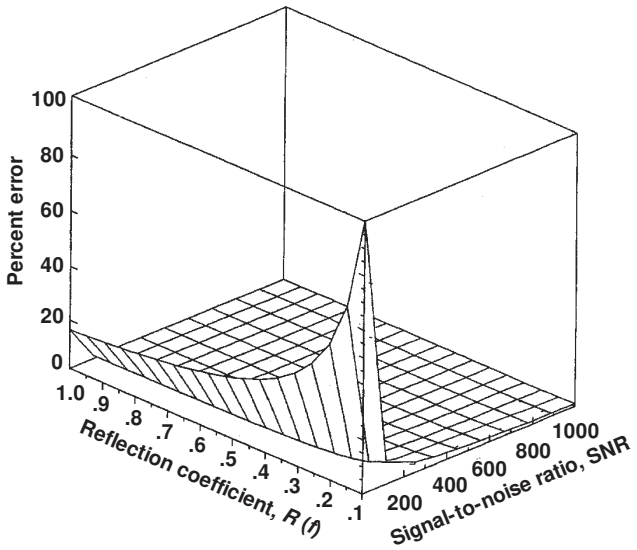

Figure 32.—Percent error associated with pulse-echo reflection coefficient measurements.

The percent error in the attenuation coefficient α measurement was calculated from

$$\%\mathrm{ERR}_\alpha = \left(\frac{\sigma_\alpha}{\alpha}\right)100 = 100\left(\frac{1}{2X\alpha}\right)\left(\frac{1}{\mathrm{SNR}}\right) \times\left[\left\{\frac{\left[\exp(4X\alpha)\right]\left[R^2+\exp(4X\alpha)\right]}{\left(1-R^2\right)^2}+1\right\} \times\left(\frac{1}{R^2}\right)+1+\left(\mathrm{SNR}^2\right)\left(4\alpha^2\right)\left(\sigma_X^2\right)\right]^{0.5} \tag{22}$$

where σ_α is the error in the attenuation coefficient measurement, X is sample thickness, σ_X is the error in the thickness measurement (3×10^{-4} cm in this investigation), R is the reflection coefficient, and SNR is the signal-to-noise ratio. Figure 33 shows the percent error associated with pulse-echo attenuation coefficient measurement. Error in α is low for intermediate values of R and low values of α. It increases greatly for $R \le 0.1$ and $R \ge 0.9$ and as α increases.

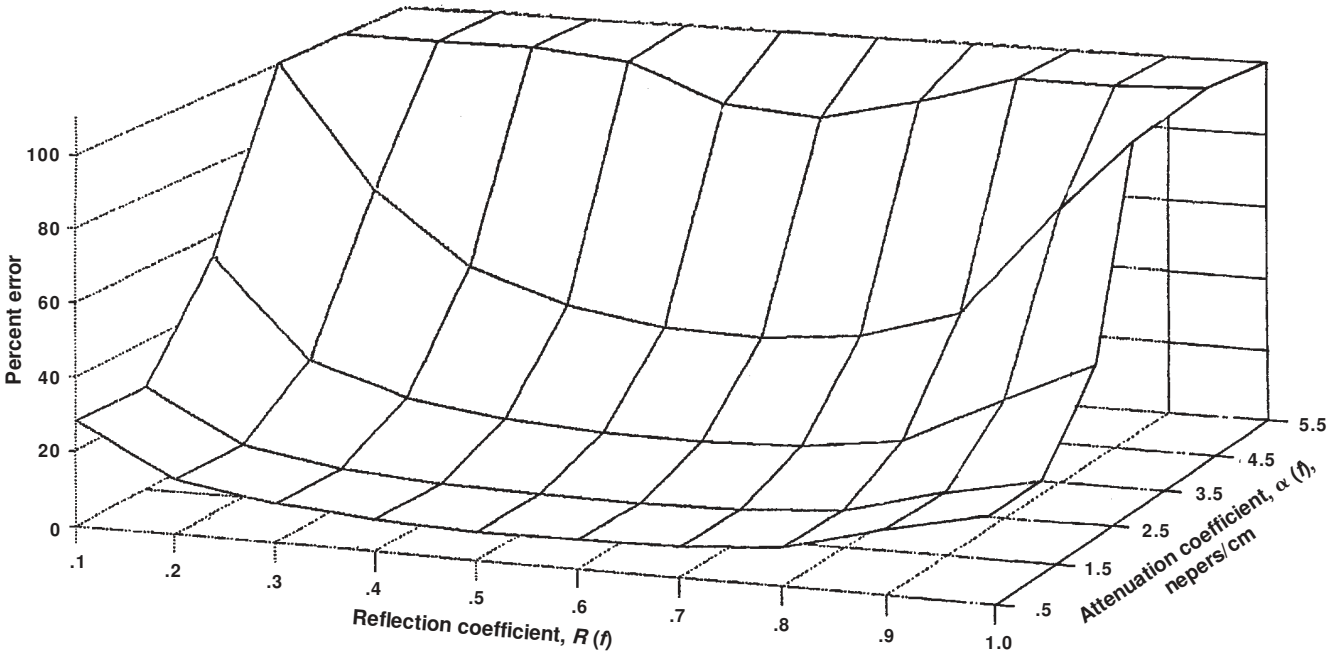

Figure 33.—Percent error associated with pulse-echo attenuation coefficient measurements. SNR = 250; X = 0.3 cm; $\sigma_X = 3 \times 10^{-4}$ cm.

Appendix B
Fabrication of Si_3N_4 Samples

Processing

The microstructure and properties of Si_3N_4-based materials depend on the processing methods. In this investigation, seven near-theoretical-density β-Si_3N_4 disk-shaped samples (labeled SN1 to SN7) were manufactured from two batches of starting powder according to the following procedures (ref. 41). The starting powder composition was 91.7 g Kemanord Si_3N_4 + (1.9 g SiO_2 + 6.2 g Y_2O_3) densification additives. Two batches of powder were milled in ethanol with Si_3N_4 media in sintered reaction-bonded Si_3N_4 solid mills for 100 hr. The milled slurries were sieved through a 10-μm sieve and then combined in a large plastic bottle. The powders were allowed to settle for about one week. Then, excess ethanol was removed by carefully pouring the fluid from the container. The bottle containing the slurry was shaken and then small samples of the slurry were placed in weighing dishes, weighed, dried, and then weighed again in order to determine the solids loading (in volume percent) of the slurry. A bottle containing slurry was then placed in a hot water bath in order to evaporate some of the excess ethanol. A 15 vol % solids slurry was obtained. The bottle containing the slurry was tumbled for 16 hr. Forty pieces of Si_3N_4 media were added to provide mixing, but no further particle size reduction was expected. The pH of the slurry was raised to 10 by the addition of ammonium hydroxide (NH_4OH).

Slurry pressing was used to consolidate the samples. Disk-shaped samples were formed under 9-MPa pressure in a die. The slurry charge was compacted between filter-paper disks, which trapped the solids. Porous stainless steel disks were used above the top filter paper and below the bottom filter paper for uniform pressure application and expulsion of liquid. After careful drying to avoid cracking, the disks were sealed with evacuated thin-wall plastic tubing. Cold isostatic pressing under 414-MPa pressure was performed to increase green density.

The disks were placed in a tungsten cup with a loose-fitting lid and sintered at 2140 °C for 4 hr under 5-MPa nitrogen pressure. Disks 1 to 4 were sintered in one run, and disks 5 to 7 were sintered in another run. Sintering was done in a tungsten-mesh-element, all-refractory-metal, water-cooled, double-wall furnace. High-purity boron nitride setters separated the disks from each other and from the tungsten cup.

Machining and Polishing

Machining was accomplished in two steps. First, a rough machining with coolant was performed in which the thickness of the samples was reduced from approximately 0.5 cm to 0.3 cm, and the top and bottom surfaces were made flat and parallel within ±25 μm by using a 20-μm diamond wheel. Then, the samples were machined by using the same size diamond wheel so that top and bottom surfaces were made flat and parallel to ±2 μm. An average of less than 0.02 cm of material was removed from the samples in this step. Five samples then were lapped on one side to obtain a fine polish by using successively 45-, 30-, 15-, 9-, 6-, and 3-μm diamond slurry. Each lapping took approximately 2 hr. The samples were cleaned with acetone after polishing. Figure 9 shows typical surface profiles for machined and polished surfaces of the Si_3N_4 disks. Machined disk surfaces were characterized by less than 1-μm peak-to-peak roughness. No difference in surface condition between polished regions at a disk center and at a high-pore-fraction area were observed.

Appendix C
Symbols

a	pore radius; scatter radius
$B_j(F)$	Fourier transformed $B_i(t)$ where $i = 1, 2$
$B_i(t)$	time-domain ultrasonic echo off sample back surface where $i = 1, 2$
D	grain size
$\%\mathrm{ERR}_i$	percent error in i where i = velocity, reflection coefficient, or attenuation coefficient
$\mathrm{FS}_i(F)$	Fourier transformed $\mathrm{FS}_i(t)$ where $i = 1, 2$
$\mathrm{FS}_j(t)$	time-domain ultrasonic echo off sample front surface where $i = 1, 2$
f	frequency
k	wavenumber
n_o	number of scatterers per unit volume
P	pore fraction; position
R	reflection coefficient
$R(f)$	frequency-dependent reflection coefficient
SNR	signal-to-noise ratio
V	velocity
V_L	longitudinal wave velocity
$V_p(f)$	frequency-dependent phase velocity
V_{pulse}	pulse velocity determined from cross-correlation method
V_S	shear-wave velocity
V_0	velocity in fully dense material
X	sample thickness
Z	acoustic impedance
α	attenuation coefficient
$\alpha(f)$	frequency-dependent attenuation coefficient
γ	scattering cross section
γ_N	normalized scattering cross section
θ	phase angle
λ	wavelength
ν	Poisson's ratio
ρ	density
σ	error
τ	time delay between two ultrasonic pulses
τ_o	time delay between two ultrasonic pulses determined from cross-correlation

Subscripts:

0	no pores
1, 2, 3	buffer rod, couplant, and sample, respectively

References

1. Metals Handbook. Ninth ed., Vol. 17: Nondestructive Evaluation and Quality Control. ASM International, Metals Park, OH, 1989.
2. Vary, A.: NDE of HITEMP Composites—Status and Needs. HITEMP Review 1992, NASA CP–10104, Vol. III: Turbine Materials, 1992, pp. 75–1 to 75–14. (Permission to use this material was granted by Hugh Gray on Feb. 10, 1993.)
3. McCauley, J.W.: Materials Testing in the 21st Century. Nondestructive Testing of High-Performance Ceramics: Conference Proceedings, A. Vary and J. Snyder, eds., American Ceramic Society, Westerville, OH, 1987, pp. 1–18.
4. Baaklini, G.Y.; and Sanders, W.A.: Correlation of Processing and Sintering Variables With the Strength and Radiography of Silicon Nitride. Adv. Ceram. Mater., vol. 3, 1988, pp. 88–94.
5. Ellingson, W.A., et al.: Magnetic Resonance Imaging: A New Characterization Technique for Advanced Ceramics. Am. Ceram. Soc. Bull., vol. 68, June 1989, pp. 1180–1186.
6. Generazio, E.R.; Roth, D.J.; and Baaklini, G.Y.: Acoustic Imaging of Subtle Porosity Variations in Ceramics. Mater. Eval., vol. 46, Sept. 1988, pp. 1338–1343.
7. Cramer, E., et al.: The Application of Thermal Diffusivity Imaging to SiC-Fiber-Reinforced Silicon Nitride. Presented at the Conference on Quantitative Nondestructive Evaluation, University of California, San Diego, LaJolla, CA. July 19–24, 1992.
8. Kunnerth, D.C.; Telschow, K.L.; and Walter, J.B.: Characterization of Porosity Distributions in Advanced Ceramics: A Comparison of Ultrasonic Methods. Mater. Eval., vol. 47, 1989, pp. 571–575.
9. Roth, D.J., et al.: Spatial Variations in A.C. Susceptibility and Microstructure for the $YBa_2Cu_3O_{7-x}$ Superconductor and Their Correlation With Room-Temperature Ultrasonic Measurements. J. Mater. Res., vol. 6, no. 10, 1991, pp. 2041–2053.
10. Stang, D.B.; Salem, J.A.; and Generazio, E.R.: Ultrasonic Imaging of Textured Alumina. NASA TM–101478, 1989.
11. Shyne, J.C.; Grayelli, N.; and Kino, G.S.: Acoustic Properties as Microstructure Dependent Materials Properties. Nondestructuve Evaluation, O. Buck and S.M. Wolf, eds., Metallurgical Society of AIME, Warrendale, PA, 1981, pp. 133–146.
12. Kino, G.S., et al.: Acoustic Measurements of Stress Fields and Microstructure. J. Nondestruct. Eval., vol. 1, 1980, pp. 67–77.
13. Birks, A.S.; Green, R.E.; and McIntere, P.: Second ed., Vol. 7: Ultrasonic Testing. American Society for Nondestructive Testing, Columbus, OH, 1991, pp. 237, 389–830, 852.
14. Roth, D.J., et al.: Review and Statistical Analysis of the Ultrasonic Velocity Method for Estimating the Porosity Fraction in Polycrystalline Materials. NASA TM–102501, 1990.
15. Generazio, E.R.: The Role of the Reflection Coefficient in Precision Measurement of Ultrasonic Attenuation. Mater. Eval., vol. 43, no. 8, 1985, pp. 995–1004.
16. Generazio, E.R.; and Roth, D.J.: Ultrasonic Imaging of Porosity Variations Produced During Sintering. J. Am. Ceram. Soc., vol. 72, no. 7, 1989, pp. 1282–1285.
17. Richerson, D.W.; and Stephan, P.M.: Evolution of Applications of Si_3N_4-Based Materials. Mater. Sci. Forum, vol. 47, 1989, pp. 282–307.
18. New Structural Materials Technologies: Opportunities for the Use of Advanced Ceramics and Composites—A Technical Memorandum. Report OTA–TM–E–32, U.S. Congress, Office of Technology Assessment, Washington, DC, 1986.
19. Bulijan, S.T.; and Baldoni, J.G.: Silicon Nitride-Based Composites. Mater. Sci. Forum, vol. 47, 1989, pp. 249–266.
20. Breazeale, M.A.; Cantrell, J.H.; and Heymann, J.S.: Ultrasonic Wave Velocity and Attenuation Measurements. Methods of Experimental Physics, Vol. 19: Ultrasonics, P.D. Edmonds, eds., Academic Press, New York, 1981, pp. 67–135.
21. Hull, D.R.; Kautz, H.E.; and Vary, A.: Measurement of Ultrasonic Velocity Using Phase-Slope and Cross-Correlation Methods. Mater. Eval., vol. 43, no. 11, 1985, pp. 1455–1460.
22. Kingery, W.D.; Bowen, H.K.; and Uhlman, D.R.: Introduction to Ceramics. John Wiley & Sons, New York, 1976, p. 770.
23. Lynnworth, L.C.: Ultrasonic Measurements for Process Control: Theory, Techniques, Applications. Academic Press, New York, 1989, pp. 113–114.
24. Hsiao, C.P.; and Kline, R.A.: The Measurement of Viscoelastic Moduli Using an Ultrasonic Spectroscopy Technique. 1984 IEEE Ultrasonics Symposium; Proceedings, IEEE, New York, 1984, pp. 443–446.
25. Christensen, R.M.: Theory of Viscoelasticity, An Introduction. Academic Press, New York, 1969.
26. Sayers, C.M.: Ultrasonic Velocity Dispersion in Porous Materials. J. Phys. D: Appl. Phys., vol. 14, 1981, pp. 413–420.
27. Birring, A.S.; and Hanley, J.J.: Effect of Cavities on Ultrasonic Attenuation and Velocity. Nondestructive Characterization of Materials II, J.F. Bussiere, et al., eds., Plenum Press, New York, 1987, pp. 673–681.
28. Kinsler, L.E., et al.: Fundamentals of Acoustics. John Wiley & Sons, New York, 1982, p. 128.
29. Truell, R.; Elbaum, C.; and Chick, B.B.: Ultrasonic Methods in Solid State Physics. Academic Press, New York, 1969, pp. 162–178.
30. Evans, A.G., et al.: Ultrasonic Attenuation in Ceramics. J. Appl. Phys., vol. 47, no. 5, 1978, pp. 2669–2679.
31. Sachse, W; and Pao, Y.H.: On the Determination of Phase and Group Velocities of Dispersive Waves in Solids. J. Appl. Phys, vol. 49, no. 8, 1978, pp. 4320–4327.
32. Hull, D.R.; Leonhardt, T.A.; and Sanders, W.A.: Plasma Etching a Ceramic Composite. NASA TM–105430, 1991.
33. Papadakis, E.P.: Ultrasonic Diffraction From Single Apertures With Application to Pulse Measurements and Crystal Physics. Physical Acoustics; Principles and Methods, Vol. XI, W.P. Mason, ed., Academic Press, New York, 1975, pp. 151–211.
34. Nair, S.M.; Hsu, D.K.; and Rose, J.H.: Porosity Estimation Using the Frequency Dependence of the Ultrasonic Attenuation. J. Nondestruct. Eval., vol. 8, no. 1, 1989, pp. 13–26.
35. Shen, P.; and Houghton, J.R.: Ultrasonic Attenuation Measurement and Its Application in Porosity Evaluation of Composite Materials. Presented at the American Society Nondestructive Testing 1992 Spring Conference, Orlando, FL, Mar. 30–Apr. 3, 1992.
36. MSC/NASTRAN User's Manuial, Ver. 64. MacNeal-Schwendler Corporation, Los Angeles, CA, 1984, pp. 24–187.
37. Enginering Property Data on Selected Ceramics, Vol. I: Nitrides. Metals and Ceramics Information Center, Columbus, OH, 1976, pp. 5.3.3–5, 5.3.3–18.
38. Ziegler, G.: Thermo-mechanical Properties of Silicon Nitride and Their Dependence on Microstructure. Mater. Sci. Forum, vol. 47, 1989, pp. 162–203.
39. Teagle, P.R.: Nondestructive Evaluation of Composite Aerospace Components. Composite Materials in Aircraft Structures, D.H. Middleton, ed., Wiley, New York, 1990, pp. 200–214.
40. Bevington, P.R.: Data Reduction and Error Analysis for the Physical Sciences, Ch. 4. McGraw-Hill, New York, 1969.
41. Sanders, W.A.; Kiser, J.D.; and Freedman, M.R.: Slurry-Pressing Consolidation of Silicon Nitride. NASA TM–101365, 1988.

REPORT DOCUMENTATION PAGE

Form Approved
OMB No. 0704-0188

1. AGENCY USE ONLY (*Leave blank*)	2. REPORT DATE	3. REPORT TYPE AND DATES COVERED
	August 1993	Technical Paper

4. TITLE AND SUBTITLE

Quantitative Mapping of Pore Fraction Variations in Silicon Nitride Using an Ultrasonic Contact Scan Technique

5. FUNDING NUMBERS

WU–506–43–11

6. AUTHOR(S)

Don J. Roth, James D. Kiser, Suzanne M. Swickard, Steven A. Szatmary, and David P. Kerwin

7. PERFORMING ORGANIZATION NAME(S) AND ADDRESS(ES)

National Aeronautics and Space Administration
Lewis Research Center
Cleveland, Ohio 44135–3191

8. PERFORMING ORGANIZATION REPORT NUMBER

E–7558

9. SPONSORING/MONITORING AGENCY NAME(S) AND ADDRESS(ES)

National Aeronautics and Space Administration
Washington, D.C. 20546–0001

10. SPONSORING/MONITORING AGENCY REPORT NUMBER

NASA TP–3377

11. SUPPLEMENTARY NOTES

Don J. Roth, James D. Kiser, and Suzanne M. Swickard, NASA Lewis Research Center. Steven Szatmary and David Kerwin, Cleveland State University, Cleveland, Ohio 44115, and NASA Resident Research Associates at Lewis Research Center. Responsible person, Don J. Roth, (216) 433–6017.

12a. DISTRIBUTION/AVAILABILITY STATEMENT

Unclassified - Unlimited
Subject Category 38

12b. DISTRIBUTION CODE

13. ABSTRACT ***(Maximum 200 words)***

An ultrasonic scan procedure using the pulse-echo contact configuration was employed to obtain maps of pore fraction variations in sintered silicon nitride samples in terms of ultrasonic material properties. Ultrasonic velocity, attenuation coefficient, and reflection coefficient images were obtained simultaneously over a broad band of frequencies (e.g., 30 to 110 MHz) by using spectroscopic analysis. Liquid and membrane (dry) coupling techniques and longitudinal and shear-wave energies were used. The major results include the following: Ultrasonic velocity (longitudinal and shear wave) images revealed and correlated with the extent of average through-thickness pore fraction variations in the silicon nitride disks. Attenuation coefficient images revealed pore fraction nonuniformity due to the scattering that occurred at boundaries between regions of high and low pore fraction. Velocity and attenuation coefficient images were each nearly identical for machined and polished disks, making the method readily applicable to machined materials. Velocity images were similar for wet and membrane coupling. Maps of apparent Poisson's ratio constructed from longitudinal and shear-wave velocities quantified Poisson's ratio variations across a silicon nitride disk. Thermal wave images of a disk indicated transient thermal behavior variations that correlated with observed variations in pore fraction and velocity and attenuation coefficients.

14. SUBJECT TERMS

Ultrasonics; Velocity; Attenuation; Silicon nitride; Spectroscopy; Microstructure; Pore fraction; Nondestructive testing

15. NUMBER OF PAGES

40

16. PRICE CODE

A03

17. SECURITY CLASSIFICATION OF REPORT	18. SECURITY CLASSIFICATION OF THIS PAGE	19. SECURITY CLASSIFICATION OF ABSTRACT	20. LIMITATION OF ABSTRACT
Unclassified	Unclassified	Unclassified	